

Chapter 7

Composite Electrolyte for All-Solid-State Lithium Battery



Jie Zhang, Yafang Zhang, and Jingtao Wang

7.1 Introduction

All-solid-state lithium batteries (ASSLBs) have been considered as next-generation energy storage devices owing to the remarkable energy density and high safety as compared with conventional batteries [1, 2]. Solid-state electrolytes (SSEs) are the key component of ASSLBs, and their ionic conductivity and mechanical stability directly determine the battery performance [3]. Generally, the SSEs can be divided into inorganic ceramic electrolyte and polymer electrolyte [3–5].

Among the reported SSEs, solid polymer electrolytes, represented by poly(ethylene oxide) (PEO), possess the advantages of high processability, flexibility, and low cost [6]. However, the strong crystallinity limits its Li-ion conductivity (10^{-8} – 10^{-6} S cm⁻¹ at room temperature) [4]. Recently, the strategy of preparing hybrid polymer electrolytes using nanofillers and polymer matrix can maximize the advantages of nanomaterials and polymer matrix, which can effectively improve the ionic conductivity and stability of SSEs [7–9]. In general, the addition of highly stable inorganic nanosheets (e.g., graphene oxide, montmorillonite, montmorillonite, MXene, and boron nitride) into PEO matrix can significantly improve the mechanical strength of SSEs, although the crystallinity of polymer matrix is reduced [10–13]. Meanwhile, the organic–inorganic interfaces formed in the electrolyte can provide high-efficiency pathways for Li⁺ transfer and thus endow the electrolyte with high ionic conductivity [14]. For instance, Luo and co-workers used vermiculite nanosheets to prepare composite polymer electrolyte [15], which utilized the

J. Zhang · Y. Zhang · J. Wang (✉)

School of Chemical Engineering, Zhengzhou University, Zhengzhou 450001, P. R. China

e-mail: jingtaowang@zzu.edu.cn

J. Wang

Henan Institute of Advanced Technology, Zhengzhou University, Zhengzhou 450003, P. R. China

functional groups on functionalized nanosheets to improve the interfacial Li^+ conductivity. Thus, a high ionic conductivity of $2.9 \times 10^{-5} \text{ S cm}^{-1}$ was achieved at room temperature.

On the other hand, inorganic ceramic electrolytes with surface oxygen vacancy and periodic crystal structure possess excellent ionic conductivity, wide electrochemical windows, and outstanding stability [3, 16, 17]. Despite the excellent Li^+ transfer performance of inorganic ceramic electrolytes, large thicknesses are usually required to ensure the mechanical stability of electrolytes owing to mechanical brittleness [18]. Meanwhile, the large interfacial resistance between the electrolyte and electrodes also limits the battery performance. Organic–inorganic composite could subtly combine the excellent ionic conductivity of inorganic electrolyte with the excellent compatibility and processability of polymer electrolyte to enhance the Li^+ transfer capacity and mechanical stability of electrolyte [19, 20]. Nevertheless, the advantages of fast ionic conductor cannot be fully maximized in composite electrolyte due to the tendency of ceramic particles to agglomerate and the difficulty of forming continuous transfer pathways [21]. Therefore, the electrolytes with bicontinuous phase structure, including metal–organic frameworks (MOFs) [22], covalent organic frameworks (COFs) [23], and ceramic networks [24], have exhibited enormous competitiveness. These structures show intrinsic advantages of high specific surface areas, tailorable porosity, and continuous transfer channels [25]. For instance, Zekoll et al. constructed a solid electrolyte with continuous transfer pathways using 3D ceramic framework, which exhibited high ionic conductivity ($1.6 \times 10^{-4} \text{ S cm}^{-1}$ at 25 °C) and excellent mechanical stability [26].

In this chapter, we introduce lithiated polydopamine-modified GO nanosheet (LiDGO) hybrid polymer electrolyte [27], poly(ethylene glycol) grafted polymer-like quantum dots (PPQDs) hybrid polymer electrolyte [28], composite electrolyte with PEO-threaded MOF nanosheets [29], 3D LLTO framework/PEO composite electrolyte [30], 2D thin LLTO framework/PEO composite electrolyte [31], and 2D lamellar LLTO/Vr composite electrolyte [32] for all-solid-state lithium batteries. The microstructure and electrochemical properties of these composite electrolytes are investigated in detail.

7.2 Composite Electrolyte with Lithiated GO

GO nanosheets were prepared by improved Hummers' method, in which graphite powders were oxidized and exfoliated [33]. 2.0 g GO nanosheets were added to 2 mg mL^{-1} dopamine-containing aqueous solution, immersed in Tris and HCl controlled solution at $\text{pH} = 8.5$, and stirred for 3 h at room temperature to obtain DGO nanosheets. DGO powders were then obtained by centrifugation at 9000 rpm [34]. Then, the above DGO powders were added to LiOH solution (1 M). After stirring for 48 h, it was washed with deionized water for several times and centrifuged at 9000 rpm to collect the powder and ensure no residual LiOH. After freeze-drying for 48 h, LiDGO powders were successfully prepared.

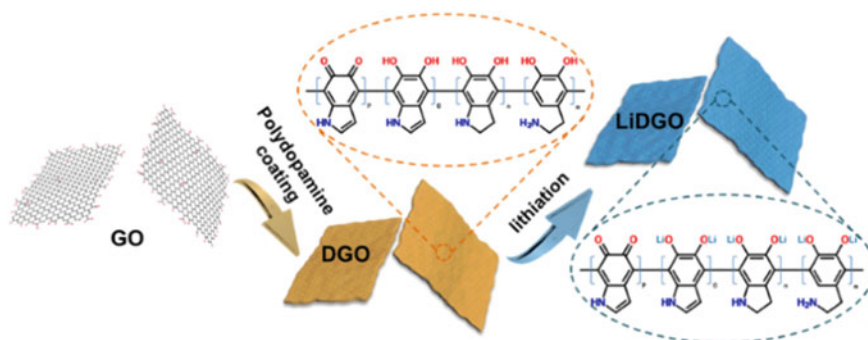


Fig. 7.1 Preparation process of LiDGO nanosheet. Copyright (2021), Elsevier [27]

According to the solution casting technique, solid-state polymer electrolytes (SPEs) were obtained. PEO was mixed with bis(trifluoromethane)sulfonamide lithium salt (LiTFSI) (EO/Li = 20: 1) in acetonitrile. LiDGO, GO, or DGO was dissolved in acetonitrile. These two solutions were mixed and stirred for 12 h to obtain casting solution, and then cast on a polytetrafluoroethylene plate. After drying for 48 h at 50 °C in a vacuum oven, the SPEs were prepared. All SPEs were stored in the glove box filled with argon.

Figure 7.1 shows that LiDGO nanosheets were obtained by lithiation of anchored Ar-OH groups on DGO nanosheets. DGO nanosheets were prepared through the self-polymerization of dopamine on the surface of GO nanosheets [35–37]. Then, lithium ions were introduced to the surface of nanosheets by replacing hydrogen on hydroxide radicals with lithium ions. Considering that the LiDGO nanosheets are completely cleaned after lithiation process, strong interaction between Li⁺ and DGO nanosheet is speculated.

Considering the mechanical stability and ionic conductivity, LiDGO nanosheets were added to PEO-LiTFSI casting solution with a loading capacity of 6 wt% to prepare SPE. At the same time, GO and DGO nanosheets were added into SPE, respectively, for comparison. Figure 7.2a, b demonstrates that the LiDGO nanosheets are uniformly distributed in the polymer matrix, and no obvious agglomeration of nanosheet is observed. And the SPE has an average thickness of about 120 μm.

This organic–inorganic hybridization combines the advantage of the flexibility of PEO and dimensional stability of LiDGO, resulting in excellent mechanical properties of PEO/LiTFSI/LiDGO. After poking treatment and exposure to violent stretching, PEO/LiTFSI/LiDGO can retain its integrality (Fig. 7.3a). As shown in Fig. 7.3b, stress–strain testing result exhibits that the tensile strength and elongation at break of PEO/LiTFSI/LiDGO are 1.25 MPa and 936%, respectively, 2.4 times and 1.3 times higher than those of blank PEO/LiTFSI. The hardness and modulus of PEO/LiTFSI/LiDGO are 1.4 times and 1.5 times higher than those of blank PEO/LiTFSI, respectively. These mechanical properties will help as-prepared SPE to improve the inhibition ability of lithium dendrite growth [38–40].

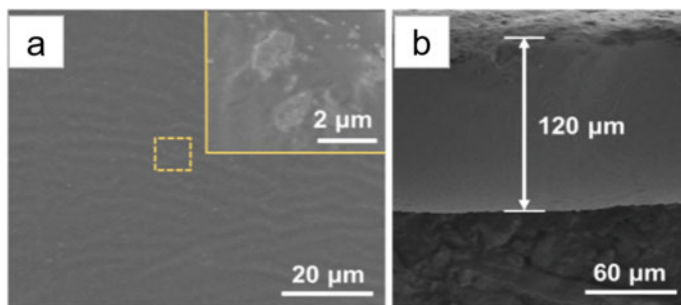


Fig. 7.2 **a** Surficial SEM image of PEO/LiTFSI/LiDGO. **b** Cross-sectional SEM image of PEO/LiTFSI/LiDGO. Copyright (2021), Elsevier [27]

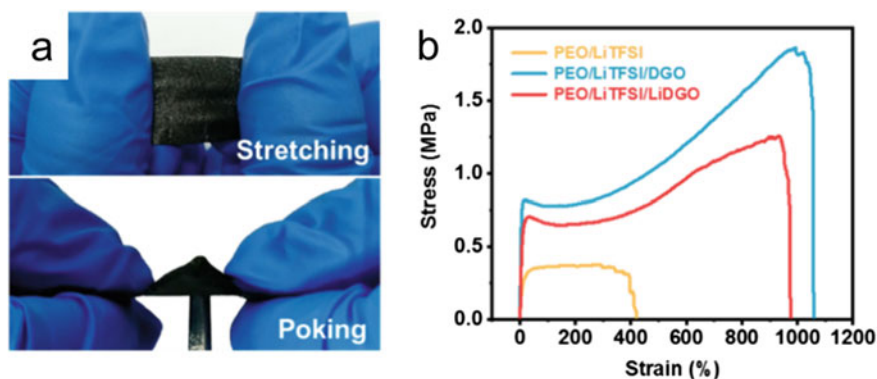


Fig. 7.3 **a** Undergoing stretching and poking of photographs of PEO/LiTFSI/LiDGO. **b** Stress-strain curves of PEO/LiTFSI/LiDGO, PEO/LiTFSI/DGO, and PEO/LiTFSI electrolytes. Copyright (2021), Elsevier [27]

It is worth noting that the mechanical property of PEO/LiTFSI/DGO is superior to that of PEO/LiTFSI/LiDGO due to the strong hydrogen bond interactions between PEO chains and DGO nanosheets, which is weakened by the presence of lithium ions in PEO/LiTFSI/LiDGO. The results of differential scanning calorimetry (DSC) could confirm this speculation. Compared with PEO/LiTFSI/DGO, the melting point (T_m) and glass transition temperature (T_g) of PEO/LiTFSI/LiDGO decline by 2.0 °C and 1.6 °C, respectively (Fig. 7.4a, b). These indicate that the LiDGO-PEO interactions are weakened and the motility of PEO chain is enhanced. The crystallinity of PEO in electrolyte was calculated according to the melting enthalpy [41]. X-ray diffractometry (XRD) results further prove that the chain motility of PEO/LiTFSI/LiDGO is stronger than that of PEO/LiTFSI/DGO, which shows obviously lower peak intensity than PEO/LiTFSI and PEO/LiTFSI/DGO [42]. The ionic conductivity of the SPE can be enhanced through newly formed amorphous regions and the construction of organic-inorganic interfaces in PEO.

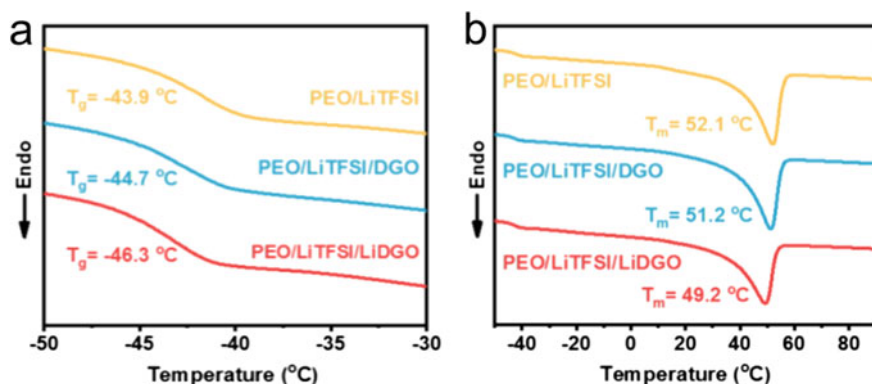
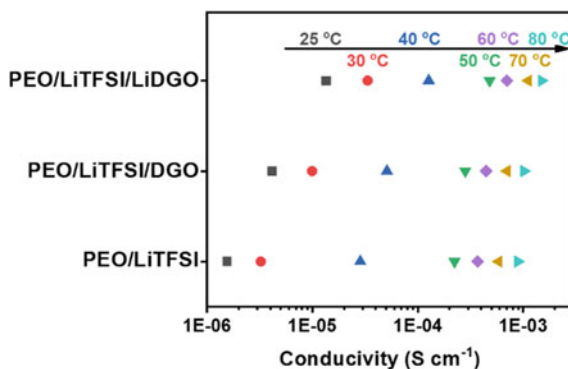


Fig. 7.4 The DSC thermograms of PEO/LiTFSI/LiDGO, PEO/LiTFSI/DGO, and PEO/LiTFSI at **a** -30 to -50 °C and **b** 90 to -50 °C. Copyright (2021), Elsevier [27]

Figure 7.5 displays the ionic conductivities of the as-prepared electrolytes. At 30 °C, the ionic conductivity of PEO/LiTFSI is 3.2×10^{-6} S cm^{-1} , and the conductivity increases with the increase of testing temperature. The addition of nanosheets enhances ionic conduction of SPE as compared with PEO/LiTFSI. At 30 °C, the ionic conductivity of PEO/LiTFSI/LiDGO and PEO/LiTFSI/DGO reaches 3.4×10^{-5} and 9.9×10^{-6} S cm^{-1} , which are ten and two times higher than that of PEO/LiTFSI, respectively. The enhanced conductivity mainly results from the construction of long-range interfacial transfer channels in SPE and the reduction of crystallinity, which provide low-energy-barrier pathways for fast Li-ion conduction.

Activation energy (E_a) data confirm this speculation. The E_a value of electrolytes below T_m is obtained through fitting ionic conductivity data of electrolytes at different temperatures, which are then calculated using Arrhenius equation [43]. For PEO/LiTFSI, PEO/LiTFSI/DGO, and PEO/LiTFSI/LiDGO electrolytes, the E_a value below T_m is 1.59, 1.34, and 1.19 eV, respectively. In addition, according to Vogel-Tamman-Fulcher equation, the E_a value of electrolytes above T_m is obtained

Fig. 7.5 The ionic conductivities of PEO/LiTFSI/LiDGO, PEO/LiTFSI/DGO, and PEO/LiTFSI electrolytes. Copyright (2021), Elsevier [27]



[44, 45]. Compared to the E_a value for PEO/LiTFSI above T_m (0.10 eV), the value for PEO/LiTFSI/DGO decreases to 0.09 eV. E_a value of PEO/LiTFSI/DGO may be reduced due to the construction of long-range interfacial transfer channels. However, the E_a value of PEO/LiTFSI/LiDGO is further decreased to 0.08 eV when it has the same nanosheet loading amount as PEO/LiTFSI/DGO. We hypothesize that the decrease of E_a value for PEO/LiTFSI/LiDGO is due to free Li^+ concentration augment. This is because ionic conductivity of solid-state electrolyte depends not only on the continuity of conduction pathway, but also on the concentration of lithium ion in the conduction pathway. Therefore, Fourier transform infrared (FTIR) was used to detect the degree of dissociation of lithium salts, in which the bonded LiTFSI ion pairs and free TFSI⁻ correspond to peaks at $\sim 744\text{ cm}^{-1}$ and $\sim 739\text{ cm}^{-1}$, respectively [46–48]. The LiTFSI dissociation degree for PEO/LiTFSI/DGO increases to 88.7% compared with that of PEO/LiTFSI (81.1%). This phenomenon may be due to existence of DGO in SPE, in which abundant amine and hydroxyl groups on DGO could promote LiTFSI to dissociate into more free lithium ions through Lewis acid–base interactions. For PEO/LiTFSI/LiDGO, the dissociation degree of LiTFSI further improves to 95.7% as compared with PEO/LiTFSI/DGO. PEO/LiTFSI/LiDGO has the same loading amount of nanosheet but higher ionic conductivity (3.4×10^{-5}). The conductivity is much higher than that of PEO/LiTFSI/DGO ($9.9 \times 10^{-6}\text{ S cm}^{-1}$), indicating that PEO/LiTFSI/LiDGO has a higher LiTFSI dissociation degree. This is related to the lithiation of DGO. The hydroxyl and amine groups on DGO have Lewis acid–base interactions with LiTFSI to promote its dissociation, thus providing a large amount of Li^+ on the surface of LiDGO. And the zeta potential vibration of LiDGO nanosheet further confirms this phenomenon, as seen from Fig. 7.6b. In acetonitrile solution, when the weight ratio of LiTFSI–LiDGO increases from 0 to 12, the zeta potential of LiDGO nanosheet changes from -40 to 20 mV . These indicate that the concentration of Li^+ in LiDGO–PEO interface is effectively elevated owing to the enrichment of free Li^+ on surface of LiDGO rather than the random distribution in PEO matrix [44, 49]. Therefore, the ionic conductivity and Li^+ transference number of PEO/LiTFSI/LiDGO are significantly enhanced by the locally enriched free Li^+ and the constructed long-range interfacial transfer channels.

Then, in order to evaluate the operation stability during Li plating/stripping process, the electrolytes were assembled into Li symmetrical cells. And there are significant lithium dendrites on the Li electrode surface, which are attributed to the difference of the ionic conductivity induced by crystal in electrolyte, Li^+ heterogeneous deposition on Li electrode, as well as the weak mechanical and structural stability of PEO/LiTFSI electrolyte [50, 51]. In comparison, Fig. 7.7 shows that the addition of LiDGO and DGO nanosheets significantly improves mechanical strength and reduces the crystallinity of SPEs. Therefore, the cycling performances of batteries are improved dramatically. The cell assembled with PEO/LiTFSI/DGO electrolyte possesses better mechanical property, but poor battery cycling performance as compared with PEO/LiTFSI/LiDGO. Specially, serious short circuit occurs after cycling for 880 h in PEO/LiTFSI/DGO cell. This is attributed to the higher crystallinity in PEO/LiTFSI/DGO electrolyte, which leads to heterogeneous Li^+ deposition on Li electrode, resulting in the uncontrolled formation of

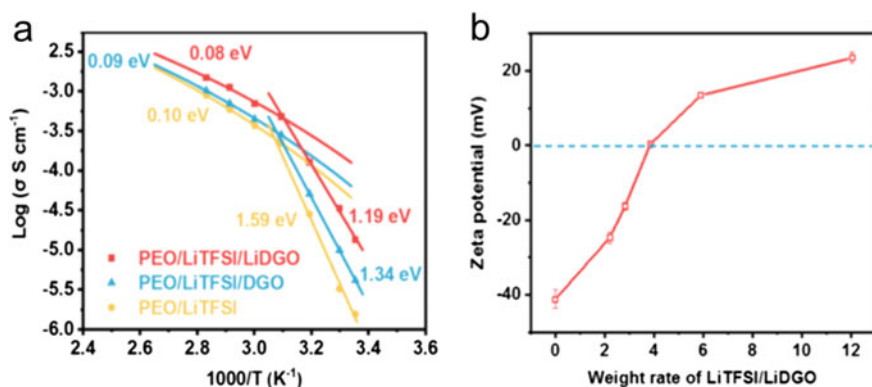


Fig. 7.6 **a** The Arrhenius plots of PEO/LiTFSI/LiDGO, PEO/LiTFSI/DGO, and PEO/LiTFSI. **b** Zeta potential of LiDGO nanosheets in acetonitrile suspension as a weight ratios function of LiTFSI/LiDGO. Copyright (2021), Elsevier [27]

lithium dendrite growth. Generally, the cell assembled with PEO/LiTFSI/LiDGO exhibits no short circuit during the 1000 h cycling, and there is no obvious lithium dendrite on corresponding Li electrode. The symmetrical cell assembled with PEO/LiTFSI/LiDGO shows excellent electrochemical performance, even when the charge/discharge duration is extended and the operating current density is increased. The Li|PEO/LiTFSI|Li symmetrical cell encounters short circuit at 98 h at 0.2 mA cm^{-2} , and Li|PEO/LiTFSI/DGO|Li symmetrical cell suffers short circuit for 134 h at 0.4 mA cm^{-2} . By comparison, the Li|PEO/LiTFSI/LiDGO|Li symmetrical cell could work normally for 200 h at 0.4 mA cm^{-2} . Moreover, during cycling, the overpotential of Li|PEO/LiTFSI/LiDGO|Li symmetrical cell is lower than those of Li|PEO/LiTFSI|Li and Li|PEO/LiTFSI/DGO|Li symmetrical cells. Such findings are attributed to the fact that the assembled cell with PEO/LiTFSI/LiDGO possesses high Li^+ transference number and ionic conductivity, and also good electrochemical stability.

As shown in Fig. 7.8a, the capacity of LFP|PEO/LiTFSI|Li cell decreases rapidly at $45 \text{ }^\circ\text{C}$ and 0.5C , and after 200 cycles, the discharge capacity decreases from 157 mAh g^{-1} to 139 mAh g^{-1} . In comparison, after 200 cycles, the discharge capacity of LFP|PEO/LiTFSI/LiDGO|Li cell is 156 mAh g^{-1} and a capacity retention of over 98% is achieved. Figure 7.8b exhibits that the polarization voltage of LFP|PEO/LiTFSI/LiDGO|Li cell is only 0.23 V after 200 cycles, which is basically the same as that at 100 cycles. Compared with that of LFP|PEO/LiTFSI|Li cell (0.28 V after 200 cycles), the polarization voltage declines significantly. These results indicate that PEO/LiTFSI/LiDGO displays excellent electrochemical stability. Meanwhile, the rate performance of the cell assembled with PEO/LiTFSI/LiDGO is also improved due to the reduction of concentration polarization in the cell, resulting from the high Li^+ transference number and ionic conductivity [52]. Figure 7.8c shows that the discharge capacity of cell assembled with PEO/LiTFSI electrolyte decreases sharply as the rate increases. In comparison, LFP|PEO/LiTFSI/LiDGO|Li

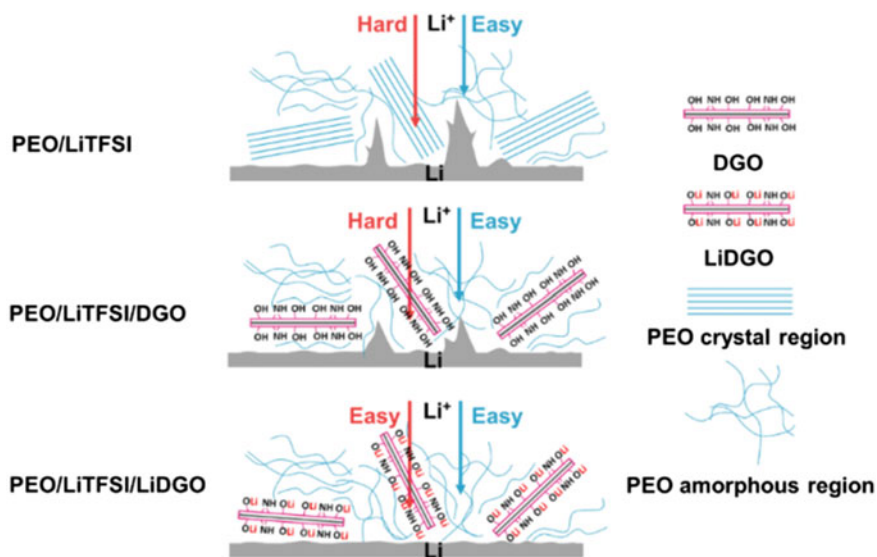


Fig. 7.7 The schematic diagram of Li deposition behaviors in different batteries. Copyright (2021), Elsevier [27]

cell presents better battery rate performances. And the discharge capacities of 161, 153, 149, 146, 143, 138, 132, and 125 mAh g⁻¹ are achieved at 0.2, 0.5, 0.8, 1, 1.2, 1.5, 1.8, and 2.0C, respectively. At the same time, Fig. 7.8d shows that the polarization voltage of LFPIPEO/LiTFSI/LiDGO/Li cell displays the small change tendency as the rate increase. It is worth noting that the rate and cycling performances of LFPIPEO/LiTFSI/LiDGO/Li cell are superior to those of most reported SPEs.

In addition, NCM523/PEO/LiTFSI/LiDGO/Li cell was assembled and operated with high-voltage window of 2.7–4.3 V. Figure 7.9a shows that NCM523/PEO/LiTFSI/LiDGO/Li cell is activated after 11 cycles under 0.2C. The cell has high discharge capacity of 128 mAh g⁻¹ and low polarization at 0.5C after 100 cycles. The discharge capacity of cell reaches to 60 mAh g⁻¹ even under a high rate of 3C (Fig. 7.9b). These indicate that PEO/LiTFSI/LiDGO displays a good electrochemical stability at high voltage and has broad application prospect in high-performance power rechargeable Li batteries.

In addition, Fig. 7.10 shows that the LFPIPEO/LiTFSI/LiDGO/Li pouch cell could power LEDs even after corner cut or folding, demonstrating the potential utilization of PEO/LiTFSI/LiDGO in safe and flexible solid-state batteries.

In conclusion, a functionalized PEO/LiTFSI/LiDGO polymer electrolyte is prepared by combining PEO matrix with LiDGO nanosheets prepared by lithium synthesis of anchored Ar-OH on DGO nanosheets. PEO/LiTFSI/LiDGO has highly enhanced mechanical stability, probably attributed to the good dispersibility of nanosheets and the inherent advantages of organic–inorganic hybridization. At the

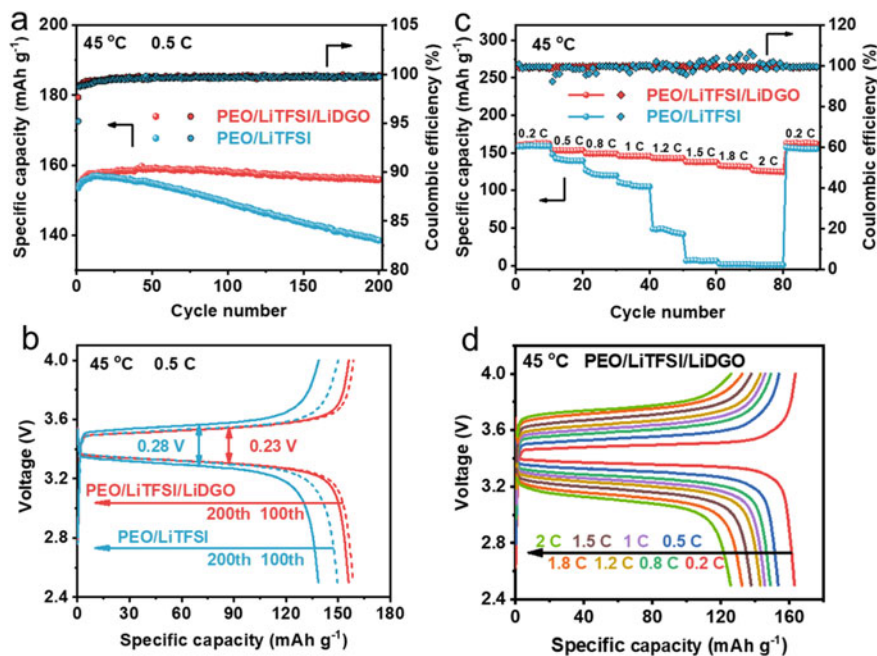


Fig. 7.8 Performances of all-solid-state cell. **a** The Coulombic efficiency and special capacity of LFP/Li cells as function of cycle number at 0.5C. **b** The charge/discharge curves of LFP/Li cells at 100th and 200th cycles. **c** The rate performances of LFP/Li cells at various rates. **d** The initial charge/discharge curves of cell assembled with PEO/LiTFSI/LiDGO at various rates. Copyright (2021), Elsevier [27]

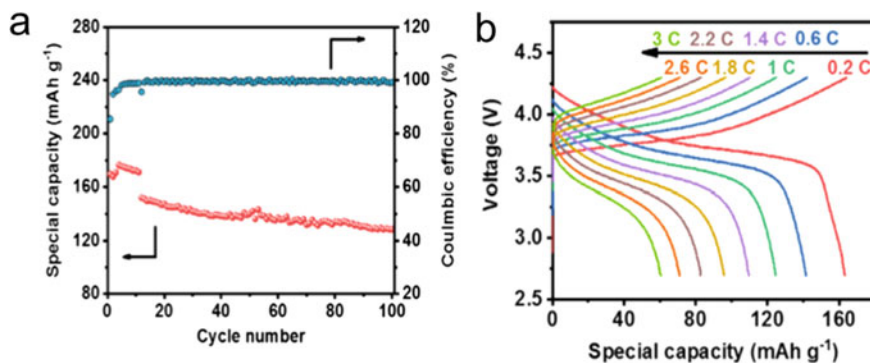


Fig. 7.9 **a** The cycling performance of NCM523|PEO/LiTFSI/LiDGO|Li cell. **b** The initial charge/discharge curves at various rates. Copyright (2021), Elsevier [27]

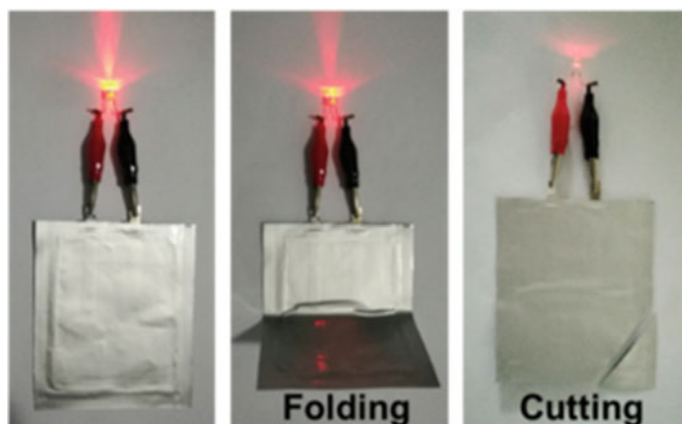


Fig. 7.10 Optical photograph of the solid-state Li/LFP pouch cell operated with folding and cutting. Copyright (2021), Elsevier [27]

same time, the introduction of LiDGO nanosheets significantly enhances concentration of local Li^+ and elevates dissociation degree of lithium salt at PEO-LiDGO interfaces. The highly enhanced Li^+ transference number and ionic conductivity for PEO/LiTFSI/LiDGO are ascribed to the conduction of long-range conductive highways of Li^+ with locally concentrated lithium ions. The discharge capacity after 200 cycles of the all-solid-state Li/LFP batteries is as high as 156 mAh g^{-1} , and the capacity retention is over 98%. This strategy may open up a new way to solve the balance problem between mechanical stability and ionic conductivity of SPEs.

7.3 Composite Electrolyte with Quantum Dot

Polymer-like quantum dots (PQDs) were prepared using literature method [53]. By optimizing PQD synthesis method, poly(ethylene glycol) grafted polymer-like quantum dots (PPQDs) were obtained. First step is to dissolve 0.96 g citric acid in 2.0 mL water. Meanwhile, ultrasonic treatment of 400 μL poly(ethylene glycol) diglycidyl ether (PEGDGE) and 540 μL diethylenetriamine was conducted at room temperature for 30 min, followed by heating to open the epoxy ring at 90 $^\circ\text{C}$ for 12 h [54, 55]. Then, the above solution was added to citric acid aqueous solution and mixed with ultrasonic for 30 min and microwave with 750 W for 2 min. Remaining unreacted small molecules were washed with 98% W/W ethanol for several times, followed by freeze-drying for 48 h to obtain yellow PPQDs powder (Fig. 7.11).

Solid-state polymer electrolytes (SPEs) were obtained using solution casting method. PPQDs, PEO, and LiTFSI were added in acetonitrile to prepare casting solution and casted on a custom polytetrafluoroethylene (PTFE) mold. The above solution was dried for 24 h in an atmosphere of argon at 30 $^\circ\text{C}$, followed by drying

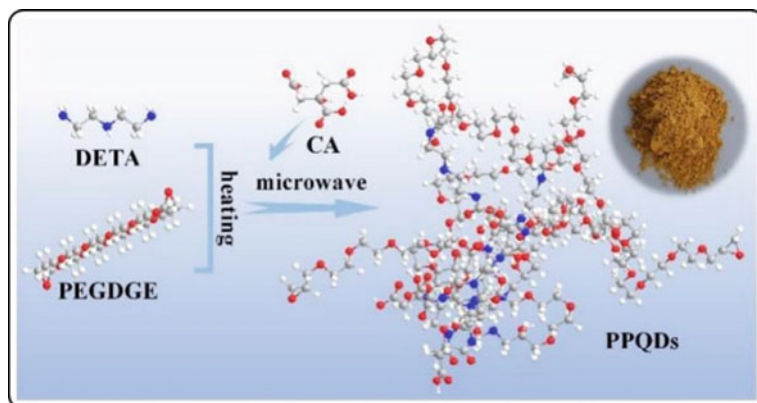


Fig. 7.11 PPQDs formation diagram. Copyright (2021), Elsevier [28]

for 24 h in a vacuum oven at 60 °C to obtain electrolyte. These pre-prepared SPEs are named as PEO/LiTFSI (0 wt% PPQDs) and PEO/LiTFSI/PPQDs (0–10 wt% PPQDs) based on the content of PPQDs. And under the same condition, PEO/LiTFSI/PQDs were also prepared. Here, EO/Li⁺ molar ratio was controlled at 18:1 in all SPEs.

As shown in Fig. 7.12a, TEM image shows a lateral size of 2–3 nm for PPQDs. By grafting PEG onto PPQDs, new O–H and C–N groups and rich ether oxygen groups are introduced. Compared with PQDs, the corresponding peak integral area of PPQDs increases with the content of C–OH, C–O–C, and C–N bands, as shown in Fig. 7.12b. These collectively prove that PPQDs possess more functional groups, smaller size, and stronger interactions with PEO and lithium salts.

Then, PEO/LiTFSI/PPQDs were prepared by solution casting method. In Fig. 7.13d, cross-sectional SEM image determines that these SPEs have a thickness of around 100 μm. It is noteworthy that the solution casting of PPQDs remains

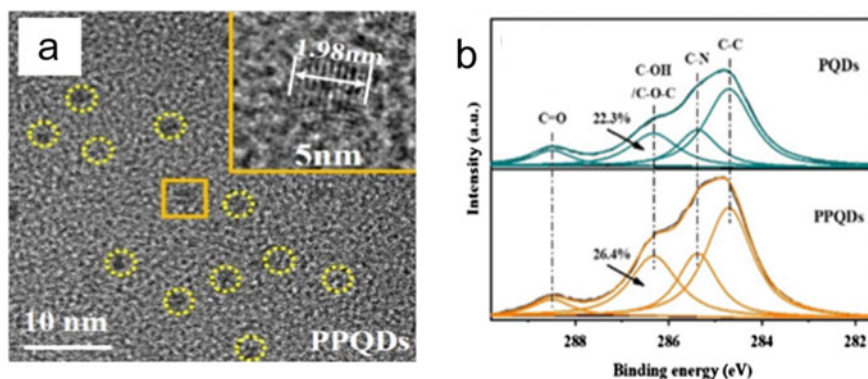


Fig. 7.12 a TEM image and high-resolution TEM image of PPQDs. b PQDs and PPQDs C 1s spectra. Copyright (2021), Elsevier [28]

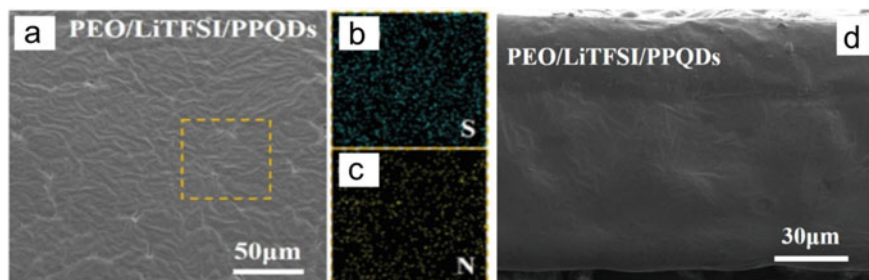


Fig. 7.13 a Surface SEM image of PEO/LiTFSI/PPQDs. EDS mappings of b S element and c N element on PEO/LiTFSI/PPQDs surface. d Cross-sectional SEM image of PEO/LiTFSI/PPQDs. Copyright (2021), Elsevier [28]

stable after long-term storage, while the solution casting of PQDs precipitates. This indicates that the compatibility between PPQDs and PEO is enhanced after grafting PEGDGE. In Fig. 7.13a, after adding PPQDs into PEO matrix, the surface SEM image of PEO/LiTFSI/PPQDs shows a smooth and uniform surface. This implies that PPQDs is evenly dispersed in PEO electrolyte due to its hydrophilic surface groups and molecular-scale size, resulting in rich PPQD-PEO interfaces and destruction of orderly PEO chain arrangement [56–59]. In addition, the PEO chain local recombination is inhibited owing to the strong hydrogen bonds formed by abundant amino and hydroxyl groups in PPQDs and the PEO chain [60]. In Fig. 7.13b, c, the uniform distribution of PPQDs in PEO matrix could be further verified by the mapping images of energy dispersion (EDS).

The electrolyte crystallization was directly determined by XRD. Figure 7.14 shows that the PEO/LiTFSI/PPQDs have the smallest characteristic diffraction peak intensity and the largest half-peak full width, implying lowest crystallinity. In addition, the intensity in XRD patterns of crystalline and amorphous phase are independent [42, 61, 62]. And the crystallinity of PEO/LiTFSI/PPQDs is 28.1% lower than that of PEO/LiTFSI (37.0%), because the PEO crystallization is effectively inhibited by the rich interfaces of PPQD-PEO.

Then, in Fig. 7.15a, b, the thermodynamic properties of different SPEs were studied by DSC analysis. By adding PPQDs, a lower enthalpy of melting (ΔH_m , 52.8 J g⁻¹ vs. 71.7 J g⁻¹ of PEO/LiTFSI) is detected, which corresponds to a lower crystallinity for PEO/LiTFSI/PPQDs electrolyte. According to the theoretical calculation, the crystallinity of PEO/LiTFSI/PPQDs is the lowest, $\chi_c = 28.5\%$, which is consistent with the XRD result. Compared with PEO/LiTFSI/PPQDs, the crystallinity of PEO/LiTFSI/PQDs is ~33% by the calculation of ΔH_m and XRD data, indicating the outstanding advantages for PPQDs. In addition, Fig. 7.15b also shows that the low glass transition temperature (T_g) of -45.6 °C further supports the low crystallinity of PEO/LiTFSI/PPQD. These results confirm that PPQDs are effective nanofillers to suppress PEO chain arrangement and crystallinity.

High flexibility and mechanical strength reduce the risk of battery short circuit by inhibiting Li dendrites. Figure 7.16a shows that the maximum displacement of

Fig. 7.14 XRD patterns of different SPEs. Copyright (2021), Elsevier [28]

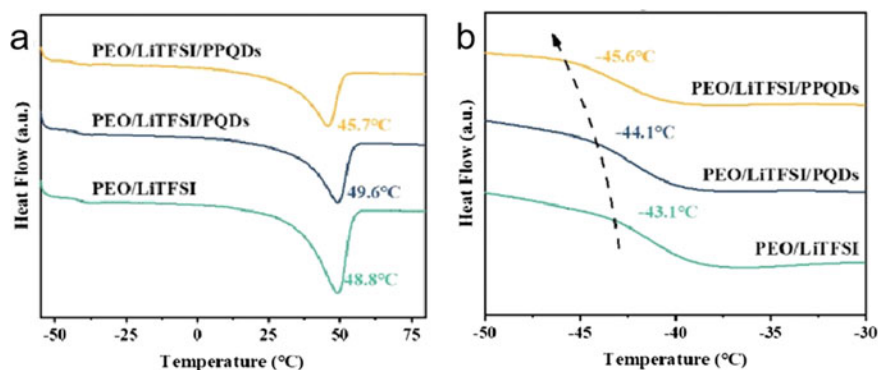
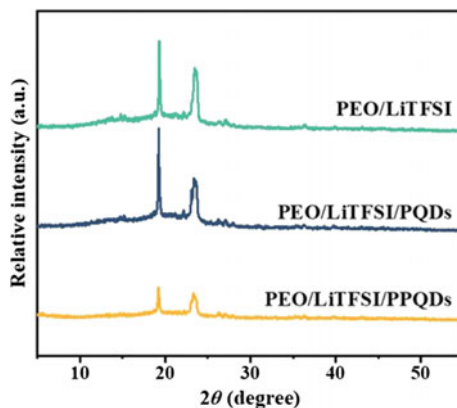


Fig. 7.15 **a** DSC heating curves of SPEs from 80 to -55 °C. **b** DSC heating curves of SPEs from -30 to -50 °C. Copyright (2021), Elsevier [28]

PEO/LiTFSI/PPQDs load–displacement curve is 2909 nm, which is 13% and 31% lower than that of PEO/LiTFSI/PQDs and PEO/LiTFSI under nanoindentation experiment, respectively. This shows that PEO/LiTFSI/PPQDs possess high mechanical modulus, which is consistent with the tensile testing results. It should be noted that PEO/LiTFSI/PPQDs has an elongation at break of 1095%, which is 25% and 46% higher than PEO/LiTFSI and PEO/LiTFSI/PQDs, respectively (Fig. 7.16b), indicating the good flexibility.

Figure 7.17 implies the ionic conductivities of different SPEs. In Fig. 7.17a, ionic conductivities of PEO/LiTFSI are 2.72×10^{-4} S cm^{-1} at 60 °C and 3.33×10^{-6} S cm^{-1} at 30 °C. By comparison, the ionic conductivities of PEO/LiTFSI/PPQDs reach 1.07×10^{-3} S cm^{-1} at 60 °C and 5.53×10^{-5} S cm^{-1} at 30 °C, which are much higher than those of PEO/LiTFSI. This significant improvement is due to the precise regulation of chemical microenvironment of PEO matrix by PPQDs, i.e., ion conductive groups, ionic coupling, and crystallinity [63, 64]. The reduction of

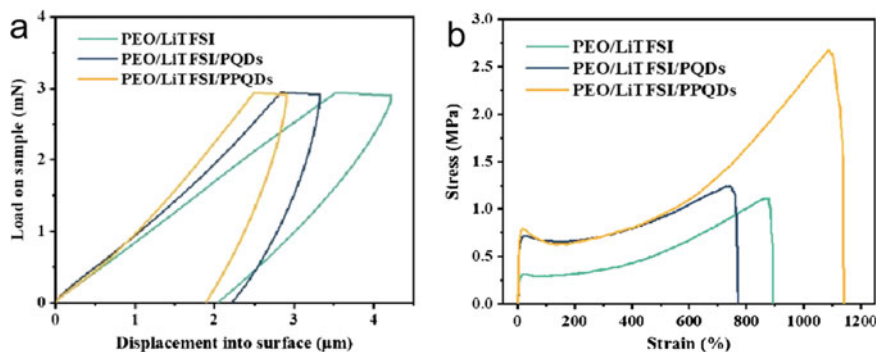


Fig. 7.16 **a** Load–displacement curves under nanoindentation test for different SPEs. **b** Stress–strain curves for different SPEs. Copyright (2021), Elsevier [28]

crystallinity provides high PEO chain mobility. Lithium salt and hydroxyl groups on PPQDs would produce strong Lewis acid–base interaction, which makes the dissociation rate reach 95.7%, providing more free Li^+ [46, 65, 66]. In addition, PPQDs can attract free Li^+ through Lewis base groups (e.g., C–O–C, C=O) and thus more free Li^+ can be quickly transferred by polyethylene glycol brushes [64]. Under the same loading, molecular-scale PPQDs can produce more interfaces of PPQD-PEO and continuous vertical networks for ion transfer when compared with large-size fillers. They collectively construct efficient networks for Li^+ transfer. In addition, in Fig. 7.17a, the E_a values of PEO/LiTFSI/PPQDs electrolyte obtained by Arrhenius fitting (1.178 eV) and Vogel–Tamman–Fulcher fitting (0.071 eV) are much lower than those of PEO/LiTFSI electrolyte (1.719 and 0.098 eV), also confirming the rapid transfer of Li^+ for PEO/LiTFSI/PPQDs electrolyte [15, 44].

As shown in Fig. 7.18a, symmetrical cells were assembled and operated at 60 °C at different current densities to evaluate the electrochemical stability of electrolyte.

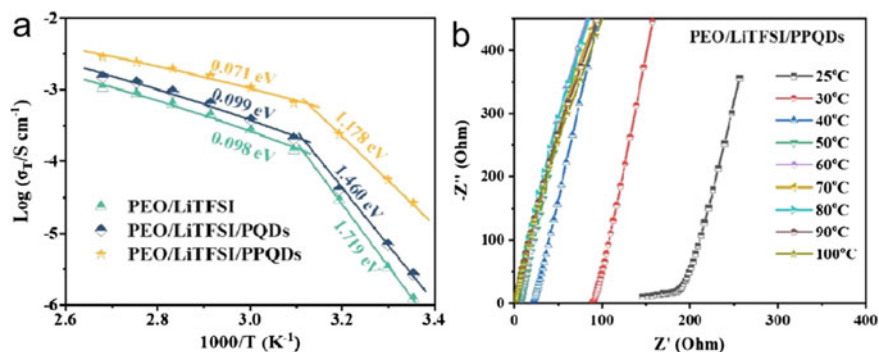


Fig. 7.17 **a** Activation energy and ionic conductivity of different SPEs. **b** Impedance spectroscopy at different temperatures of SPEs. Copyright (2021), Elsevier [28]

At 0.05 mA cm^{-2} , the Li|PEO/LiTFSI/PPQDs|Li symmetric cell displays a polarization voltage of 17 mV, much lower than that of Li|PEO/LiTFSI|Li cell (34 mV) and Li|PEO/LiTFSI/PQDs|Li cell (25 mV). It shows that PEO/LiTFSI/PPQDs have excellent interfacial contact and low internal resistance [10, 16, 67]. Notably, the voltage with Li|PEO/LiTFSI/PQD|Li or Li|PEO/LiTFSI|Li cells shows a larger irreversible drop at 0.1 and 0.2 mA cm^{-2} , respectively. This is caused by the dendrite-induced short circuits, resulting from the poor mechanical stability and uneven Li^+ deposition in Li|PEO/LiTFSI/PQD|Li and Li|PEO/LiTFSI|Li cells. SEM images of lithium surface after cycling, as shown in Fig. 7.18b, c, further verify the reason of short circuits in Li|PEO/LiTFSI/PQD|Li and Li|PEO/LiTFSI|Li cells. Under different current densities, Li|PEO/LiTFSI/PPQDs|Li cell can cycle for 1000 h and stay stable due to the efficient conduction ability of ion in PEO/LiTFSI/PPQDs, which leads to more uniform deposition of Li^+ and thus inhibits the growth of Li dendrite [67]. In Fig. 7.18d, SEM image shows compact, smooth, and uniform lithium electrode after cycling, which further confirms the high stability for Li|PEO/LiTFSI/PPQD|Li cell. In addition, the cell assembled with PEO/LiTFSI/PPQDs can continuously operate with stable overpotential for 1000 h at 60°C and 0.2 mA cm^{-2} , supporting the stability of PEO/LiTFSI/PPQDs. Therefore, the addition of PPQDs improves the ionic conductivity, flexibility, and mechanical strength of PEO/LiTFSI/PPQDs, thus ensuring excellent battery cycling stability.

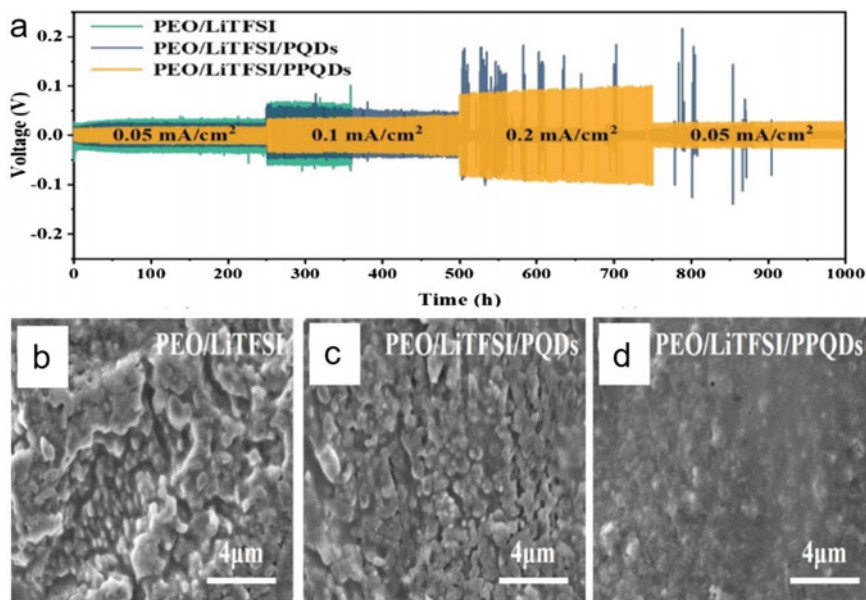


Fig. 7.18 a Voltage profiles under different current density at 60°C for Li|PEO/LiTFSI/PPQDs|Li symmetric cells. The Li electrodes surface SEM images after cycling about 1000 h obtained from b Li|PEO/LiTFSI|Li cell, c Li|PEO/LiTFSI/PQDs|Li cell, and d Li|PEO/LiTFSI/PPQDs|Li cell. Copyright (2021), Elsevier [28]

Based on the LFP|SPEs|Li cell using different electrolytes, battery performances were evaluated. In Fig. 7.19a, c, the capacity of LFPIPEO/LiTFSI/PPQDs|Li cell only reduces to $\sim 146 \text{ mAh g}^{-1}$ after 150 cycles under 1.0C. The excellent cycling stability of LFPIPEO/LiTFSI/PPQDs|Li cell is attributed to the good interfacial compatibility with electrodes, excellent physicochemical stability, and high ionic conductivity of PEO/LiTFSI/PPQDs. Furthermore, the low polarization voltage platform implies rapid Li^+ transfer capacity in PEO/LiTFSI/PPQDs [68–70]. To further highlight the advantages of PEO/LiTFSI/PPQDs, rate performances of different cells are evaluated. Notably, rate performance of LFPIPEO/LiTFSI/PPQDs|Li cell exhibits a high capacity of 142.2 mAh g^{-1} at 4.5C. When the rate returns to 0.5C, the discharge capacity recovers to 158.4 mAh g^{-1} , indicating that the LFPIPEO/LiTFSI/PPQDs|Li cell has excellent stability [70]. On the contrary, the discharge capacities of LFPIPEO/LiTFSI|Li and LFPIPEO/LiTFSI/PQDs|Li cells degrade significantly at 2.0C. This indicates that PEO/LiTFSI and PEO/LiTFSI/PQDs cannot operate at high rate, caused by low ionic conductivity and high battery polarization. The outstanding rate and cycling performances for LFPIPEO/LiTFSI/PPQDs|Li cells are attributed to structure stability and high Li^+ conduction of PEO/LiTFSI/PPQDs electrolyte.

As shown in Fig. 7.20a, the general applicability is demonstrated by the antiparallel charge–discharge capacities of LFPIPEO/LiTFSI/PPQDs|Li pouch cell. It is

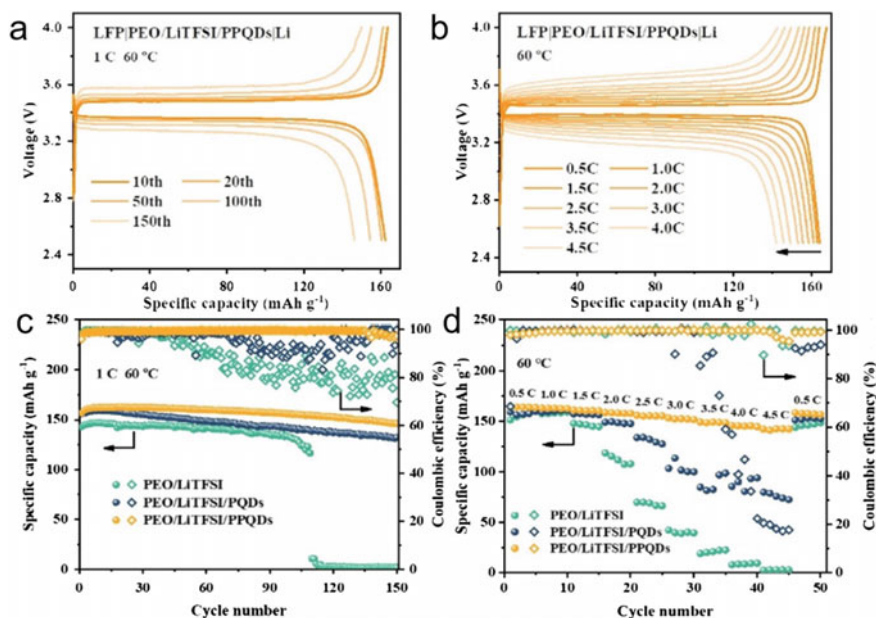


Fig. 7.19 **a** Charge–discharge voltage profiles at 1.0C and 60 °C for LFPIPEO/LiTFSI/PPQDs|Li cell. **b** Charge–discharge voltage profiles of LFPIPEO/LiTFSI/PPQDs|Li cell at 60 °C under various rates. **c** Cycling performances at 1.0C and 60 °C for LFPIPEs|Li cells. **d** Rate performances at 60 °C for LFPIPEs|Li cells. Copyright (2021), Elsevier [28]

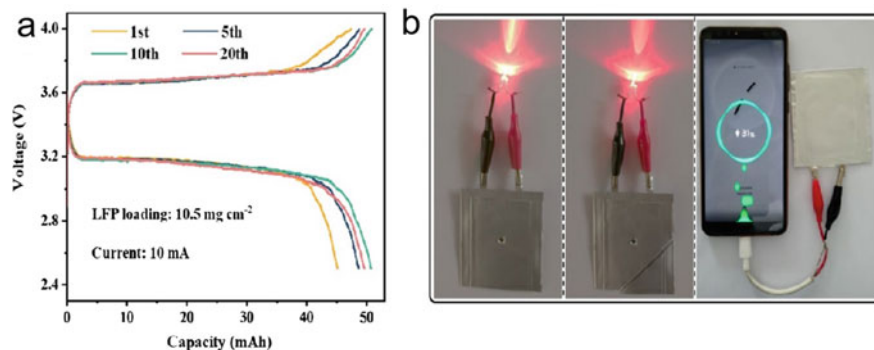


Fig. 7.20 **a** Pouch cell cycling performance of LFPIPEO/LiTFSI/PPQDs/Li. **b** Powering a phone and lighting light-emitting diode inset of all-solid-state pouch lithium batteries. Copyright (2021), Elsevier [28]

worth noting that LFPIPEO/LiTFSI/PPQDs/Li pouch cell can still light up the LED even with corner cut and nail penetration and can be acted as a successful mobile power supply (Fig. 7.20b). These results mean that the battery safety is significantly improved by using PEO/LiTFSI/PPQDs, paving the way for the development of flexible wearable batteries in the future.

In conclusion, PEG-grafted polymer-like quantum dots are synthesized as nanofillers, which possess rich functional groups and good interface compatibility with PEO chain. PPQDs are evenly dispersed in the electrolyte to form rich PPQD-PEO networks. And the lithium salt dissociation increases to 96.6%, which is attributed to the strong interaction of Lewis acid–base at the PPQD-PEO interface. Thus, continuous vertical networks for Li^+ transfer are constructed in the PEO/LiTFSI/PPQDs electrolyte, and the ionic conductivities of $1.07 \times 10^{-3} \text{ S cm}^{-1}$ at 60°C and $5.53 \times 10^{-5} \text{ S cm}^{-1}$ at 30°C are achieved. Meanwhile, the excellent flexibility and mechanical stability of the electrolyte are attributed to the hydrogen bond network formed by the PEO chains and PPQDs. Therefore, LFPIPEO/LiTFSI/PPQDs/Li cell displays excellent cycling stability of $\sim 146 \text{ mAh g}^{-1}$ at 60°C and 1.0C after 150 cycles and rate performance of $\sim 142 \text{ mAh g}^{-1}$ under at 60°C and 4.5C. In addition, such molecular-level fillers with abundant designable surface groups might exhibit great application and development potential for hydrogen-based fuel cell and all-solid-state lithium battery.

7.4 Composite Electrolyte with PEO-Threaded MOF Nanosheets

MOF nanosheets were prepared on the basis of the method in literature [71]. Firstly, 0.75 mmol 4,4'-biphenyldicarbonyl chloride was dispersed in the solution of water

(2 mL), C_2H_5OH (2 mL), and N,N -dimethylformamide (24 mL). Then, 0.8 mL triethanolamine was added to the solution. Afterward, 0.375 mmol $NiCl_2 \cdot 6H_2O$ and 0.375 mmol $CoCl_2 \cdot 6H_2O$, dissolved in 4 mL N,N -dimethylformamide, respectively, were injected into the mixture solution and stirred at 20 °C for 20 min. After that, the colloidal suspension was ultrasonicated under airtight condition for 20 h. In the end, the products were washed by 3 times by centrifugation with ethanol and subsequently dried at 25 °C, represented by MB nanosheet. Then, by replacing 4,4'-biphenyldicarbonyl chloride with TPDC, MC nanosheet was synthesized. In addition, except that 4,4'-biphenyldicarbonyl chloride was replaced by benzenedicarboxylic acid and triethanolamine was added after the injection of metal salts, the preparation step of MA nanosheet was identical to MB nanosheet's step. The lengths of A, B, and C are 6.9, 11.1, and 15.7 Å, respectively.

For the synthesis of $-NH_2$ group-modified MOF nanosheets, the nanosheets were first uniformly decentralized in 30 mL ethanol. Then, superfluous KH540 was injected slowly in the even solution. After stirring at 40 °C for 6 h, the functionalized nanosheet suspension was prepared through centrifugation and then washed by ethanol for 3 times aiming to get rid of excess reactant. Finally, at room temperature, the $-NH_2$ -modified MOF nanosheet was dried for 24 h in a vacuum oven.

The laminar composite solid electrolyte (LCSE) was synthesized by a two-step method: self-assembly and low-pressure filtrating, as shown in Fig. 7.21. The polymer can disperse uniformly in the lower and upper layers of LCSE. First, MOF nanosheets and PEO-LiTFSI with equal quality were added into acetonitrile and stirred for 4 h. Then, at room temperature, this solution was ultrasonic for 4 h, aiming to drive PEO to enter in the pores. Subsequently, the thin LCSE was prepared by filtrating the solution at low pressure on a Nylon membrane. In the end, at room temperature, the LCSE was dried for 24 h and then peeled from Nylon membrane to get the self-supporting electrolyte (PEO@N-MX LCSE). The preparation step of PEO chain intercalated LCSE (PEO/N-MB LCSE) was alike to PEO@N-MB LCSE step, except that N-MB nanosheet suspension and PEO-LiTFSI-acetonitrile solution were mixed directly and then filtrated.

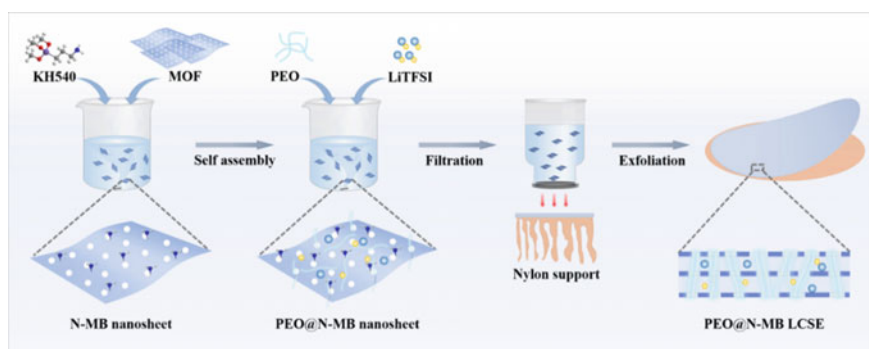


Fig. 7.21 Schematic fabrication of PEO@N-MB LCSE. Copyright (2022), John Wiley and Sons [29]

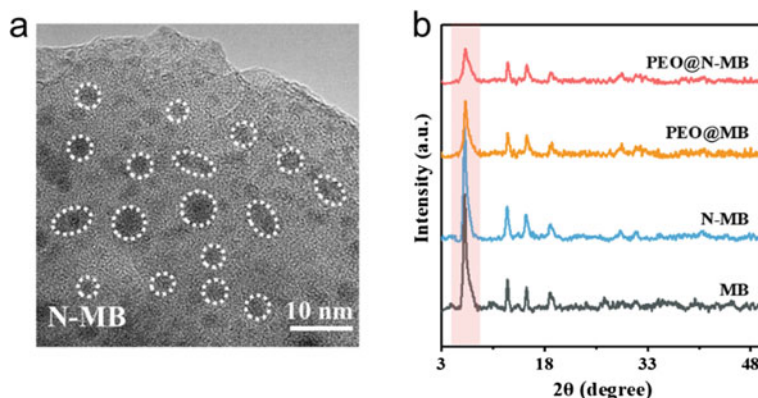


Fig. 7.22 **a** High-resolution TEM image of single N-MB nanosheet. **b** XRD patterns of PEO@N-MB, PEO@MB, N-MB, and MB nanosheets. Copyright (2022), John Wiley and Sons [29]

MOF nanosheet was fabricated by a solution of organic ligands and metal atoms using ultrasonication [71, 72]. In order to facilitate the interaction between PEO chains and MOF nanosheets and enhance the entrance of PEO into the pores of MOF nanosheets, the nanosheets were modified by silane coupling agent for grafting $-\text{NH}_2$ functional groups. TEM images in Fig. 7.22a show uniform MOF nanosheets with 2–5 nm diameter and well-distributed pores.

Then, by the two-step method, PEO-threaded MOF LCSE (PEO@N-MB LCSE) was fabricated. Firstly, the $-\text{NH}_2$ -modified MOF nanosheets were pre-assembled with PEO chains in acetonitrile to prepare PEO-threaded MOF nanosheets (PEO@N-MB). Then, XRD was used to explore the structure of them. Figure 7.22b exhibits that, for PEO@N-MB nanosheet, the peak strength at 6.5° is apparently reduced. This variation should be attributed to the disturbance derived by the PEO chains in the pores of MOF nanosheets [73]. Remarkably, PEO@N-MB nanosheets show smaller pore volume and weaker XRD peak intensity in contrast with PEO@MB nanosheets. This should result from the powerful hydrogen-bonding interactions between $-\text{NH}_2$ groups in the pores and ether oxygen groups on PEO chains, which make more PEO chains to enter into the pores of nanosheets.

Then, the PEO@N-MB nanosheet was filtrated on a Nylon membrane to prepare thin and self-supporting PEO@N-MB LCSE. In order to get defect-free stacking of even PEO@N-MB nanosheet and facilitate PEO chain to enter in the pores of nanosheets, a filtration step at low pressure was employed. Cross-sectional SEM image (Fig. 7.23a) exhibits that PEO@N-MB LCSE owns sequential layered structure which is $7.5 \mu\text{m}$ in thickness. Remarkably, the interlayer spacing of PEO@N-MB LCSE is alike to that of layered MOF framework, apparently lower than that of PEO intercalated LCSE (PEO/N-MB LCSE). These results show that most PEO chains entered into the pores rather than gathering in the channels. The porosity of PEO@N-MB LCSE was tested by BET measurement in order to confirm the

above viewpoint. Compared with PEO@N-MB nanosheet, Fig. 7.23b shows remarkably reduced porosity of PEO@N-MB LCSE. This demonstrates that, during low-pressure filtration step, PEO chains fill the pores of PEO@N-MB LCSE. Similarly, these results prove the successful preparation of MOF laminar solid electrolyte with PEO-threaded structure.

PEO@N-MB LCSE attains a high ionic conductivity owing to the PEO-threaded structure. Figure 7.24a shows that the ionic conduction of PEO@N-MB LCSE ($3.97 \times 10^{-5} \text{ S cm}^{-1}$) at room temperature is about 25 times higher than that of SPE ($1.51 \times 10^{-6} \text{ S cm}^{-1}$). On one hand, this significant advancement should be ascribed to the PEO chains inside the pores of MOF nanosheets, which give many transport paths. On the other hand, the pore confinement effect endows PEO with high chain motility, which allows fast Li^+ transport. PEO/N-MB LCSE with chemical component and alike lamellar structure exhibits a low ionic conductivity ($6.30 \times 10^{-6} \text{ S cm}^{-1}$), which deeply emphasizes the advantage of this PEO-threaded structure.

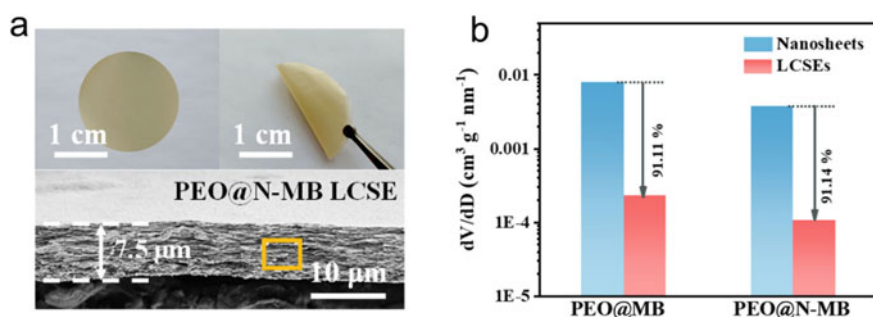


Fig. 7.23 **a** Optical and cross-sectional SEM images of PEO@N-MB LCSE. **b** Porosity of PEO@N-MB LCSE, PEO@MB LCSE, PEO@N-MB nanosheets, and PEO@MB nanosheets. Copyright (2022), John Wiley and Sons [29]

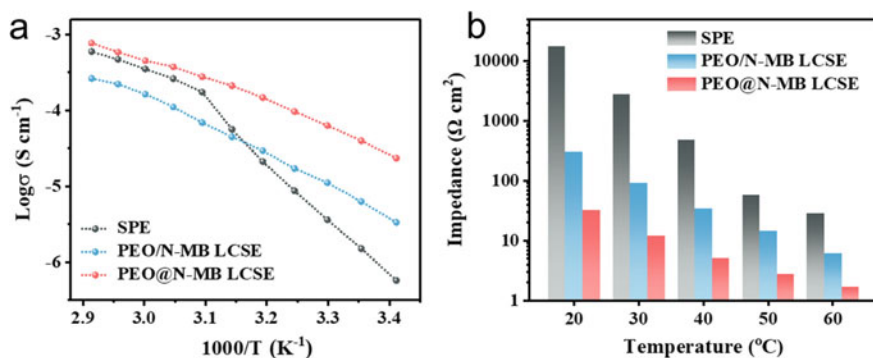


Fig. 7.24 **a** Ionic conductivity of PEO/N-MB, PEO@N-MB LCSE, and SPE. **b** ASR of PEO/N-MB, PEO@N-MB LCSE, and SPE. Copyright (2022), John Wiley and Sons [29]

PEO@N-MB LCSE owns a low area-specific resistance because of the higher ion conduction and indifferent thickness ($12 \Omega \text{ cm}^2$) at room temperature, which is two orders of magnitude lower than SPE as shown in Fig. 7.24b. Moreover, ionic transference number (t_{Li^+}) was described. The ionic transference number of PEO@N-MB LCSE reaches as high as 0.6, which is much higher than those of PEO/N-MB LCSE (0.43) and SPE (0.22). These discoveries emphasize the PEO-threaded structure with advanced chain motility, building high-efficiency transmission channels in the perpendicular direction of PEO@N-MB LCSE.

In the previous study, the chain motility and function of PEO inside the pores of nanosheets are crucially important for ionic conductivity. In order to research this detailedly, the aperture of nanosheets was tested through altering the lengths of ligands [74–76], aiming for the regulation of PEO chain configuration and purity in the pores of nanosheets. The change of pore size is proved through rejection test employing dye molecules in different sizes, which is the same as the result of aperture attained by BET test. The PEO-threaded pores were checked, as shown in Fig. 7.25a. In contrast with N-MX nanosheets, the specific surface area decreases by 77.70%, 45.92%, and 67.04% for PEO@N-MC, PEO@N-MA, and PEO@N-MB nanosheets, respectively. As MOF nanosheets have the similar weight proportion (about 50 wt%), the specific surface area of PEO@N-MC nanosheet sharply decreases, which demonstrates that more PEO chains entered into the pores as compared with N-MB and N-MA nanosheets. The diffraction peak strength of PEO@N-MC nanosheet is apparently decreased as compared to those of PEO@N-MB and PEO@N-MA nanosheets, as shown in Fig. 7.22b. And the d -spacing change of PEO@N-MC LCSE is smaller as compared with PEO@N-MB LCSE and PEO@N-MA LCSE (Fig. 7.25b), which again confirms the above viewpoint.

The ion conduction of three different LCSEs was measured detailedly. For PEO@N-MA LCSE, the ionic conductivity at 25 °C reaches $1.11 \times 10^{-5} \text{ S cm}^{-1}$ (Fig. 7.26b). In contrast, for PEO@N-MB LCSE, owing to the fact that more PEO

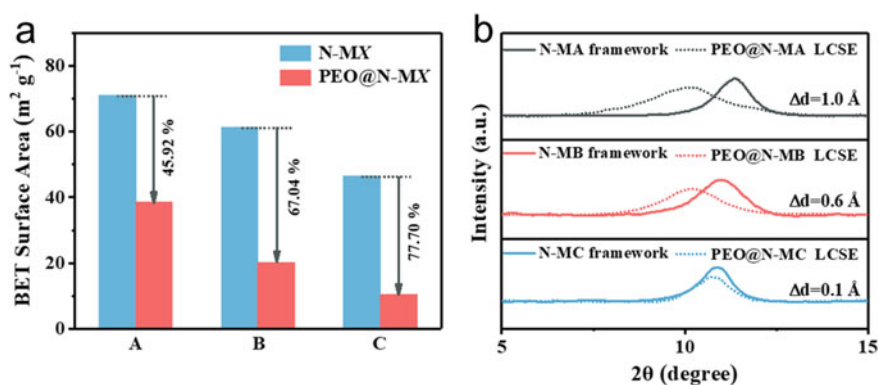


Fig. 7.25 **a** Specific surface areas of PEO@N-MX and N-MX nanosheets. **b** XRD patterns of PEO@N-MX LCSEs and N-MX frameworks. Copyright (2022), John Wiley and Sons [29]

chains enter into the pores, the ionic conductivity reaches $3.97 \times 10^{-5} \text{ S cm}^{-1}$, as shown in Fig. 7.26a. For PEO@N-MC LCSE, the conductivity achieves $1.96 \times 10^{-5} \text{ S cm}^{-1}$, despite the more PEO than other in the pores. In order to further research this finding, on the basis of the temperature-dependent conductivity curves, the transfer activation energy is calculated. It is shown that PEO@N-MC LCSE has a higher activation energy (0.123 eV) as compared with PEO@N-MB LCSE (0.114 eV), which demonstrates a high Li^+ transfer energy barrier in the former [3, 77]. These are attributed to the disorder packing of PEO chains, making Li^+ transfer paths tedious.

Because of low crystallinity of polymer chains in confined spacing, the effect on ionic conductivity can be ignored [78], and the PEO chain conformation was explored. FTIR results of PEO@N-MC, PEO@N-MB, and PEO@N-MA LCSEs were explored. The characteristic peaks of PEO at 1342, 2882, and 2945 cm^{-1} (Fig. 7.26c) correspond to wagging vibrations, symmetric stretching, and asymmetric stretching of C–H [79–81]. With the growth of PEO chains in the pores of MOF nanosheets, the peak strengths assigned to wagging vibrations and asymmetrical stretching of carbon-hydrogen bond are decreased, demonstrating the disorder degree of PEO chain [78, 82].

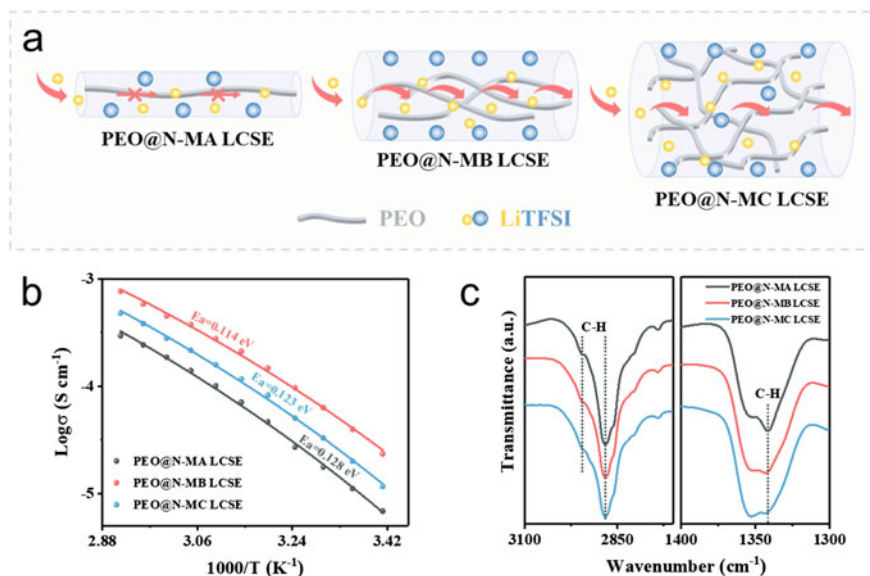


Fig. 7.26 a Concept schemes of the ion conduction of PEO@N-MB, PEO@N-MC, and PEO@N-MA LCSEs. b Ionic conductivity at different temperatures for PEO@N-MB, PEO@N-MC, and PEO@N-MA LCSEs. c FTIR absorption spectra of PEO@N-MC, PEO@N-MB, and PEO@N-MA LCSEs. Copyright (2022), John Wiley and Sons [29]

As shown in Fig. 7.27a, lithium symmetric cells were assembled and researched at 60 °C on disparate current densities. Under 0.1 mA cm⁻², the voltages of Li|PEO/N-MB LCSE|Li and Li|SPE|Li symmetric cells show stability at 24 and 31 mV, respectively, while they suffer irreversible and large drop when current density increases to 0.4 and 0.2 mA cm⁻². These suggest internal short circuit resulting from the poor mechanical strength and uneven Li⁺ deposition. In comparison, as the current densities increases from 0.1 to 0.4 mA cm⁻², the cell using PEO@N-MB LCSE can run for 800 h stably. Particularly, the overpotentials reach 45 and 22 mV at 0.2 and 0.1 mA cm⁻², respectively. For Li|PEO@N-MB LCSE|Li, the overpotential reaches 83 mV even at 0.4 mA cm⁻². The outstanding cycling performance should result from two reasons: Firstly, the outstanding ionic conductivity makes even Li⁺ deposition on the lithium metal surface and, secondly, the outstanding mechanical strength of electrolyte prevents the lithium dendrite growth efficiently. Furthermore, the electrochemical stability is assessed through LSV measurement, as shown in Fig. 7.27b. Compared with SPE (4.1 V) and PEO/N-MB LCSE (4.6 V), PEO@N-MB LCSE shows a high decomposition voltage (5.1 V). This observation resulted from the pores, which efficiently stop PEO from reacting with lithium metal. What's more, the powerful hydrogen-bonding interactions between -NH₂ functional groups of MOF nanosheets and ether oxygen of PEO chains could also prevent PEO from decomposing [83]. These also demonstrate that PEO@N-MB LCSE has great potential in high-voltage electrode materials.

LiFePO₄/Li batteries were assembled to test the rate performances and cycling performances. Figure 7.28a exhibits the cycling performances of different cells at 60 °C under 0.5C. After 74 cycles, the discharge capacity sharply drops from 130 to 0 mAh g⁻¹ for LFP|SPE|Li cell owing to the low ionic conductivity of SPE. The discharge capacity of LFP/Li cell using PEO/N-MB LCSE drops from 140 to 115 mAh g⁻¹ with a retention of 82% after 150 cycles. The promoted cycling performance is ascribed to PEO/N-MB LCSE's thin thickness and the increased lithium-ion conduction. In comparison, owing to the excellent structural stability and highest ion conduction, LFP/Li cell using PEO@N-MB LCSE owns a retention of 94% after 150 cycles and the highest initial discharge capacity (148 mAh g⁻¹).

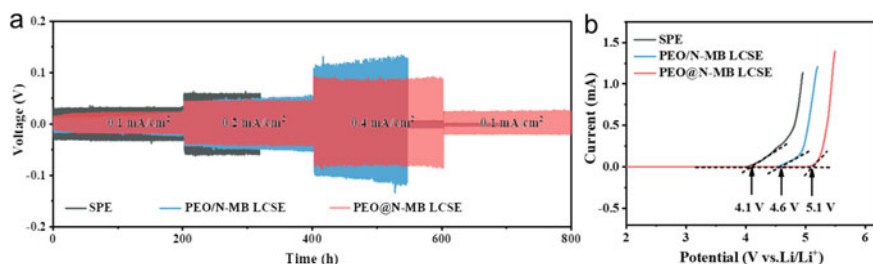


Fig. 7.27 **a** Galvanostatic cycling curves of lithium symmetric cells with SPE, PEO@N-MB, and PEO/N-MB LCSEs on different current densities at 60 °C. **b** Linear sweep voltammetry curves at 60 °C of the different electrolytes at scanning rate of 1 mV s⁻¹. Copyright (2022), John Wiley and Sons [29]

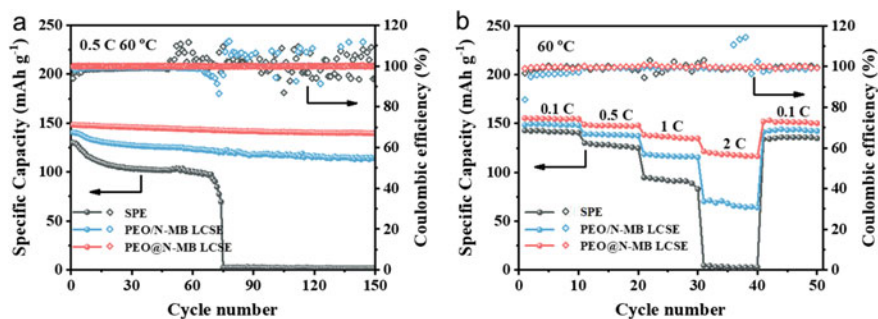


Fig. 7.28 Electrochemical performances of all-solid-state lithium battery. **a** Cycling performances of the different cells under 0.5C at 60 °C. **b** Rate performances of the different cells under various rates at 60 °C. Copyright (2022), John Wiley and Sons [29]

Additionally, the rate performances of different cells were also explored (Fig. 7.28b). The LFPISPEiLi cell has inferior Coulomb efficiency and a low discharge capacity. For LFP/Li cell using SPE, the discharge capacity drops dramatically, especially at 2.0C. For LFP/Li cell using PEO/N-MB LCSE, the discharge capacity sustains apparent recession at 2.0C while the discharge capacity of LFP/Li cell using PEO@N-MB LCSE reaches 116, 134, 148, and 154 mAh g⁻¹ at 2.0, 1.0, 0.5, and 0.1C, respectively, much higher than that of LFPISPEiLi and LFPiPEO/N-MB LCSEiLi cells under the same condition. Significantly, for LFP/Li cell using PEO@N-MB LCSE, the discharge capacity comes back to 152 mAh g⁻¹ (98.7% of the initial discharge capacity) as the current density recovers to 0.1C. These results suggest that PEO@N-MB LCSE attains outstanding stability.

In conclusion, we show the preparation and design of thin LCSE employing MOF nanosheets with PEO threading structure, as building-block through the filtration at low-pressure way. The pores are modified by -NH₂ functional groups to guide PEO chain entering in the pores of nanosheets through powerful hydrogen-bonding interactions between -NH₂ functional group and ether oxygen of PEO. Through the interactions, the threaded-PEO chains combine with the surrounding MOF nanosheets, providing PEO@N-MB LCSE (7.5 μm-thick) with outstanding mechanical stability. Furthermore, the confinement function advances the chain motility and promotes the stretching of PEO chains, endowing PEO@N-MB LCSE with improved ion conduction (3.97×10^{-5} S cm⁻¹), that is 25 times higher than PEO electrolyte. By this way, the trade-off effect is resolved between mechanical stability and ionic conductivity for PEO-based and MOF-based electrolytes. Significantly, the battery using PEO@N-MB LCSE shows a retention of 94% after 150 cycles and an outstanding initial capacity (148 mA h g⁻¹). Noticeably, we research the function of different pore sizes on the preparation of threaded-PEO chains. Then, we also confirm the superiority of synergistic function between *cis*-PEO and *trans*-PEO in promoting ionic conductivity. The excellent design approach and concept are possible to be employed to prepare other materials with polymer matrices and various aperture materials, which have great potential for ion separation, gas separation, and hydrogen-based fuel cell.

7.5 Composite Electrolyte with LLTO Framework

$\text{Li}_{0.33}\text{La}_{0.557}\text{TiO}_3$ (LLTO) framework was synthesized by sol–gel method. Generally, $\text{Ti}(\text{OC}_4\text{H}_9)_4$ (10.00 g), $\text{La}(\text{NO}_3)_3 \cdot 6\text{H}_2\text{O}$ (7.08 g), and LiNO_3 (0.74 g) were dissolved in ethanol (10 mL) and stirred at 50°C for 10 min to obtain the precursor solution [21]. Considering the thin structure and interconnected porous of nylon, it was selected as a template to prepare the LLTO framework. Subsequently, the precursor solution was mixed into nylon filter for gel permeation. Then by stirring constantly, a viscous gel was obtained. The gel-permeated nylon was dried and calcined at 1000°C for 2 h in air under a heating rate of 1°C min^{-1} . LLTO nanoparticles were prepared by the method of ball milling.

By solution-dripping method, PEO-LLTO framework (PLLF) electrolyte was prepared. LiTFSI and PEO were dried overnight at 100°C and 60°C in vacuum, respectively. LiTFSI and PEO (the molar ratio of EO to LiTFSI is 18:1) were dissolved in anhydrous acetonitrile and stirred for 4 h. Then, the solution (concentration of 1.0 g L^{-1}) was slowly dripped into the LLTO framework and then dried in a 60°C vacuum oven to remove acetonitrile completely. The drying and dripping processes were repeated many times till the bottom and top of LLTO framework were completely embedded in the PEO matrix. In addition, adding different loadings of LLTO nanoparticles into the LiTFSI and PEO solution (the molar ratio of EO to Li is 18:1) was conducted. And then, the casting solution was fully mixed and stirred for 5 h, then poured onto PTFE plate. After drying at 40°C in a vacuum, the PEO-LLTO nanoparticle (PLLN) electrolyte was prepared. All the processes of experiments were implemented in a dry glove box with argon gas. The solution of LiTFSI and PEO was completely mixed and then cast onto the PTFE plate. After drying at 40°C , the PEO (PL) electrolyte was obtained in vacuum. The processes of experiments were carried out in a glove box with argon gas. In Fig. 7.29, the synthesis procedure of PLLF electrolyte and LLTO framework is schematically illustrated.

As shown in Fig. 7.30a, the SEM image displays the PLLF electrolyte microstructure. It is observed that the LLTO framework with porous structure turns into dense electrolyte with well-organized wrinkles, implying that the PEO matrix has been infiltrated into LLTO framework. This can be supported by dimming the bright lines,

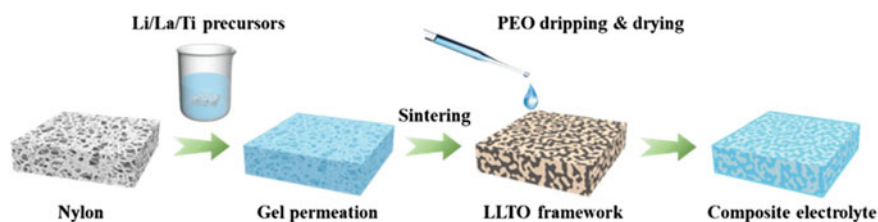


Fig. 7.29 Schematic diagram of the synthesis process of PLLF electrolyte and LLTO framework. Copyright (2021), Elsevier [30]

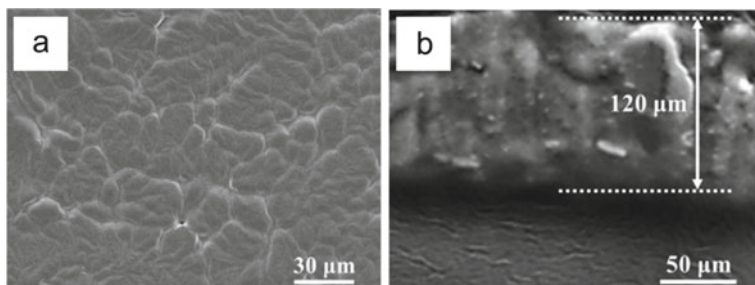


Fig. 7.30 Proofs for the synthesis of PLLF electrolyte. **a** Surface and **b** cross-sectional SEM images of PLLF electrolyte. Copyright (2021), Elsevier [30]

corresponding to the wrinkles above in the optical image [44]. In LLTO framework, the penetration of PEO is directly confirmed by cross-sectional SEM image (Fig. 7.30b), which results in uniform and dense electrolyte. This suggests that the constructed PLLF electrolyte has a structure of vertical bicontinuous phase: confined PEO and LLTO framework. Moreover, the thickness of LLTO framework is about $100\ \mu\text{m}$, which is slightly thinner than the $120\ \mu\text{m}$ of PLLF electrolyte. The excess thickness manifests that the surface of PLLF electrolyte forms a thin PEO layer. The polymer layer can restrain the side reactions between lithium anode and LLTO, and it can hold the potential to improve stability at electrolyte interface [16, 18, 84]. Herein, large pores of LLTO framework ($1\text{--}2\ \mu\text{m}$) are taken to ensure the complete entrance of PEO matrix, and therefore, it has a vertical bicontinuous phase structure. But other frameworks, like MOF and COF, fail to do so [22–24].

Thermal behaviors and chemical features of these electrolytes were researched by thermogravimetric analysis (TGA) and FTIR. The characteristic peaks of PLLF, PLLN, and PL electrolytes are fundamentally coincident as shown in FTIR [85], indicating an adequate coupling between LLTO and PEO in the fabricating process (Fig. 7.31a). Furthermore, in Fig. 7.31b, the TGA curves indicate that PL electrolyte goes through weight loss for two stages, including the evaporation of water at the first stage (below $100\ ^\circ\text{C}$), and the decomposition of lithium salt and PEO at the second stage ($380\text{--}450\ ^\circ\text{C}$). Here, during TGA test, the moisture might be from the water in the air [44]. By contrast, PLLF electrolyte shows a similar TGA curve but with a lower weight loss as compared to PL electrolyte at the second stage, implying that the LLTO framework has splendid thermal stability. The residuals for PLLF and PL electrolytes are $65.2\ \text{wt}\%$ and $6.4\ \text{wt}\%$, respectively. Thus, in PLLF electrolyte, the weight ratio of LLTO framework is about $63\ \text{wt}\%$.

For solid electrolyte, Li^+ transference number and ionic conductivity are both important indicators. The ionic conductivities of PLLN and PL electrolytes are 2.35×10^{-5} and $2.85 \times 10^{-6}\ \text{S cm}^{-1}$ at $25\ ^\circ\text{C}$, respectively, as shown in Fig. 7.32a. This finding indicates that the LLTO nanoparticles improve its transfer ability probably because of the reduction of PEO crystallization. By contrast, the ionic conductivity of PLLF electrolyte is $2.04 \times 10^{-4}\ \text{S cm}^{-1}$, 8.7, and 71.6 times greater than that of PLLN and PL electrolytes. And the conductivity remarkably precedes a lot of

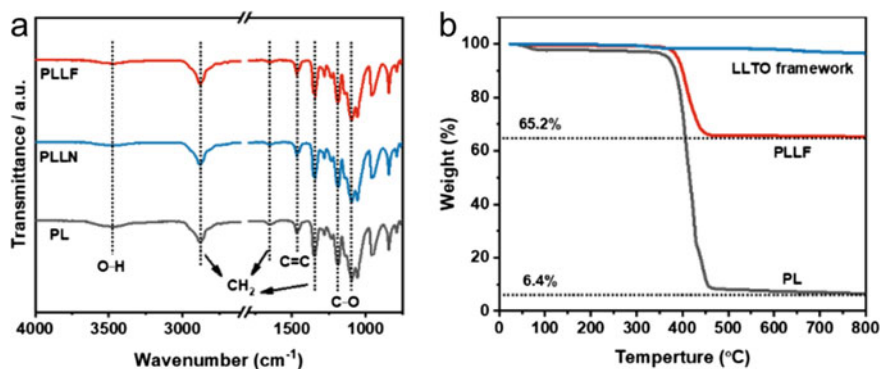


Fig. 7.31 **a** FTIR spectra of PLLF, PL, and PLLN electrolytes. **b** TGA curves of PLLF electrolytes, PL electrolytes, and LLTO framework. Copyright (2021), Elsevier [30]

electrolytes, particularly composite electrolytes, which emphasizes the advantages of structural advantage of the conductive PEO and LLTO [26].

Here, at 40 °C, the temperature turning points appear for PLLN electrolytes (Fig. 7.32b). In comparison with PL electrolyte, the reduction proves the effect of LLTO nanoparticles, which enhances the chain motion and reduces the PEO crystallization, thereby enhancing the transfer ability at relatively low temperature [86]. Moreover, the ionic conductivity of PLLN electrolyte climbs up and then declines as the LLTO mass ratio increases. In PLLN electrolyte, the decreased conductivity at high LLTO mass ratio is due to the agglomeration of substantial LLTO nanoparticles, which reduces the Li^+ transfer ability and diminishes the inhibition effect on PEO crystallization [87] while the related curve shows a straight line without distinct turning point between temperature and ionic conductivity of PLLF electrolyte. This

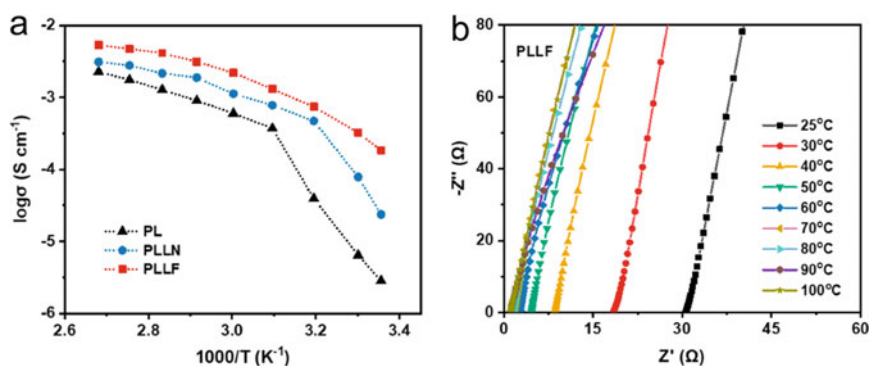
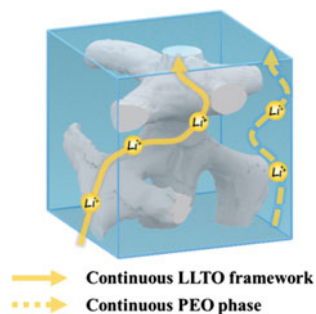


Fig. 7.32 **a** Ionic conductivity of PLLF, PLLN, and PL electrolytes at various temperatures. **b** The impedance spectra of PLLF electrolyte sandwiched by two stainless steels from 25 °C to 100 °C. Ionic conductivity is calculated through the corresponding impedance data. Copyright (2021), Elsevier [30]

Fig. 7.33 Schematic diagram of possible Li^+ conduction pathways in the PLLF electrolyte with some vertically bicontinuous transmission channels. Copyright (2021), Elsevier [30]



indicates that in this electrolyte, the Li^+ transfer follows the continuous rapid ion transfer mode [87], which implies that the limited PEO phase shows greatly improved transfer ability when compared with PLLF and PL electrolytes. Here, through a vertical bicontinuous transfer channels (particularly the LLTO framework), PLLF electrolyte acquires outstanding ionic conductivity.

Based on electrolyte structure and ionic conductivity, there are three possible transfer channels (Fig. 7.33) in this as-prepared PLLF electrolyte: PEO-LLTO interface, LLTO framework, and PEO phase [88, 89]. To test this speculation, more characteristics including the segmental motion of PEO, the crystallization, and the existence of lithium ions were conducted.

High-resolution solid-state nuclear magnetic resonance spectrometry (Li NMR) clearly exhibits three Li^+ local environments (Fig. 7.34a): PEO-LLTO interface, LLTO framework, and lithium salts in PEO phase [89, 90]. The ^6Li resonances at 2.5 and -0.3 ppm correspond to LiTFSI in LLTO framework and PEO phase, respectively. Except for these two signals, at 1.8 ppm, the PEO-LLTO interface with a characteristic signal is obtained. This implies that under this bicontinuous phase structure, both PEO and LLTO phases can transfer Li^+ effectively.

Then, the XRD performs the crystallization behavior of PEO as shown in Fig. 7.34b. It is observed that all of the diffraction peaks belong to LLTO and PEO phases present in the curve of PLLF and PLLN electrolytes. While it implies that the peak intensity of PEO phase at 23.4° and 19.0° shows prominent alteration in comparison with the excellent crystallinity in PL electrolyte. The LLTO nanoparticles are added which have steric reference to the PEO chains for reducing PEO crystallinity [88, 90, 91]. By contrast, under close chemical component, the PEO matrix exhibits much lower crystallinity degree in PLLF electrolyte. This implies that in LLTO framework the crystallization behavior of PEO is extremely inhibited, and the restricted PEO chains are difficult to condense into ordered packages. Different from the low crystallinity of PEO phase, PLLF electrolyte shows distinctly elevated crystallinity for LLTO phase relative to PLLN electrolyte, implying the well-crystallized LLTO framework [21, 92]. The weak crystallinity of PEO and the strong crystallinity of LLTO are both conducive to Li^+ conduction, and these also highlight the structural advantage of this PLLF electrolyte.

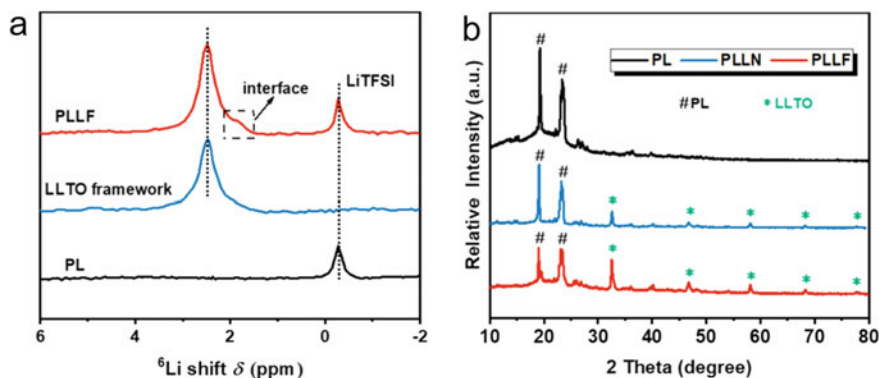


Fig. 7.34 Ion transfer characteristics of PLLF, PLLN, and PL electrolytes. **a** ^6Li NMR spectra of LLTO framework, PLLF, and PL electrolytes. **b** XRD patterns of PLLF, PLLN, and PL electrolytes. Copyright (2021), Elsevier [30]

Heterogeneous Li^+ deposition often forms dendrites on the surface of lithium anode during the operation process of lithium stripping/plating. The interface stability between solid electrolyte and anode determines the electrochemical performance of battery [10]. The constant-current cycling performance was performed at a current density of 0.1, 0.2, and 0.4 mA cm^{-2} at 60 $^\circ\text{C}$ (Fig. 7.35). The stability of Li/PLLN/Li and Li/PL/Li symmetric batteries are 28.5 mV and 41.5 mV at 0.1 mA cm^{-2} , respectively, which is higher than that of Li/PLLF/Li (20.3 mV). As the current density rises to 0.2 mA cm^{-2} , the voltage of the Li/PL/Li battery increases sharply and then suddenly drops to 0 V, suggesting a short circuit caused by lithium dendrites which pierce the electrolyte [86]. This is because of the poor mechanical stability of the electrolyte and the uneven deposition of Li^+ on the electrolyte–electrode. The others keep a steady voltage. In addition, when the current density is 0.4 mA cm^{-2} , Li/PLLN/Li symmetric cells stop working due to uneven deposition of interfacial lithium ions at high current densities. This implies that the interface between PLLN electrolyte and Li electrode is unstable. Meanwhile, the voltage of the Li/ PLLF/Li battery fluctuates slightly and there is no significant polarization. This means that Li^+ ions are evenly distributed within the electrolyte because of its double continuous transfer channels in vertical direction, which afford uniform deposition at interface and efficient Li^+ transfer [17, 93].

All-solid-state LFP/Li cells were assembled to evaluate rate performance and cycling performance. Figure 7.36 shows the cycling performance at 1.0C and 60 $^\circ\text{C}$. After 150 cycles, the discharge capacity of LFP/PLLF/Li battery decreases to 154.7 mAh g^{-1} with a retention rate of 97.2%. In comparison, the discharge capacities of LFP/PLLN/Li and LFP/PL/Li cells decrease to 137.2 mAh g^{-1} and 2.6 mAh g^{-1} , with only 88.5% and 1.9% retention, respectively. The superior cycling performance and increased capacity are probably ascribed to the synergistic effect of Li^+ conduction frame and sealed PEO, which enhance the ion transfer capacity, and the interconnect structure also improves cycling stability. The LLTO framework enables superior

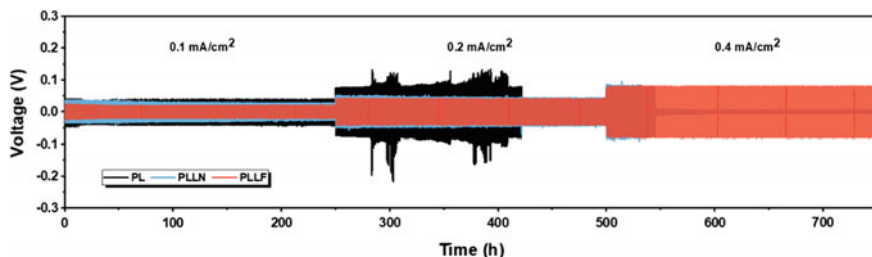


Fig. 7.35 Galvanostatic cycling performance of Li/PLLF/Li, Li/PLLN/Li, and Li/PL/Li symmetrical cells with different current densities at 60 °C. Copyright (2021), Elsevier [30]

Li⁺ transport capabilities through its vertically continuous channels. At the same time, the limited PEO phase with low crystallinity also helps the rapid Li⁺ transfer with the helped of enhanced chain movement [45, 94]. Therefore, in comparison with the other two cells, LFP/PLLF/Li cells show significantly enhanced electrochemical performance. In addition, the charge–discharge curves of LFP/PLLF/Li cells remain stable, while the polarization voltage rises gently, and the capacity decreases mildly at the current density of 1.0C. And this demonstrates the excellent stability and lithium-ion transfer of the vertical bicontinuous phase structure.

Moreover, Fig. 7.37 shows the original, 1st, 30th, and 70th cycle's impedance spectra of LFP/PLLF/Li cells at 1.0C and 60 °C. What is noteworthy is that the interfacial resistance of LFP/PLLF/Li cells changes slightly during the cycling (from 41.9 Ω at 1st cycle to 55.7 Ω at 70th cycle). This suggests that the PLLF electrolyte-Li electrode interface can maintain stable and consistent contact during the cycling without Li dendrite growth. This finding is in accordance with the constant-current cycle, as confirmed by the SEM image of the surface near Li electrode. The excellent cycling performance of LFP/PLLF/Li batteries proves the interface stability of PLLF electrolyte-Li electrodes [10, 95].

Fig. 7.36 The cycling performance of all-solid-state cells with various electrolytes. Copyright (2021), Elsevier [30]

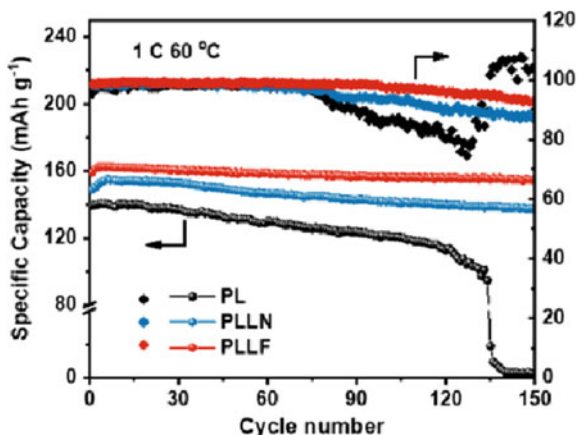
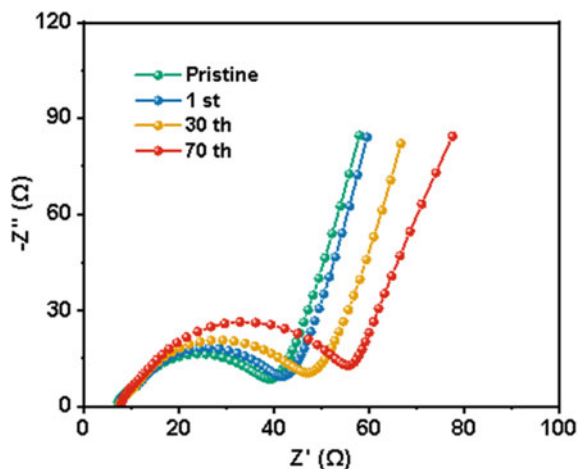


Fig. 7.37 AC impedance spectra of LFP/PLLF/Li cell after different cycles. Copyright (2021), Elsevier [30]



In conclusion, we have demonstrated a method to dramatically enhance Li^+ conductivity and improve electrolyte structure stability by constructing vertical dual-continuous transfer channels using PEO and LLTO framework. The vertically continuous frame and airtight PEO act as high-efficiency Li^+ transfer pathways, significantly improving the ion conduction property of electrolytes. Particularly, at $25\text{ }^\circ\text{C}$, PLLF electrolyte attains excellent ionic conductivity of $2.04 \times 10^{-4}\text{ S cm}^{-1}$, about 72 times higher than that of PL electrolyte and better than the majority of reported electrolytes. Besides, the PLLF electrolyte shows excellent interfacial compatibility and structural stability due to its stably interconnect network. After 150 cycles, the LFP/PLLF/Li cell demonstrates excellent cycling stability (154.7 mAh g^{-1}) and an ultra-high retention rate (97.2%). In consequence, this framework-based electrolyte with high structural stability, featuring superior conductivity and vertically bicontinuous phase structure, should be instrumental for providing a path to construct the next-generation devices for energy storage.

7.6 Composite Electrolyte with LLZO Nanosheets

$\text{Li}_7\text{La}_3\text{Zr}_2\text{O}_{12}$ (LLZO) nanosheets were synthesized using two-step sintering approach and subsequent liquid-phase exfoliation. Firstly, sucrose (0.50 g), $\text{ZrO}(\text{NO}_3)_2$ (0.46 g), $\text{La}(\text{NO}_3)_3 \cdot 6\text{H}_2\text{O}$ (1.30 g), and LiNO_3 (0.58 g) were dissolved in deionized water (70 mL), in which the pH value was kept at 1.5. The above precursor solutions were subsequently sintered at $250\text{ }^\circ\text{C}$ and $850\text{ }^\circ\text{C}$ for 4 h and 2 h, respectively [96]. The calcined product was added to an acetonitrile solution (80 mL) and stirred at room temperature for 12 h, followed by sonication for 10 min. To obtain uniformly dispersed LLZO nanosheets, the above solution was centrifuged at 1000 rpm for 15 min to remove unexfoliated particles.

LLZO laminar inorganic solid electrolyte (LLISE) was obtained by the suction filtration method. Firstly, layered LLZO frameworks were prepared by filtering the solution of LLZO nanosheets onto nylon substrates. Secondly, the binder for configuring LLZO nanosheets is a small amount of PEO and LiTFSI (18:1, EO/Li molar ratio) which was dissolved in acetonitrile. The above solution was suction filtered in a layered LLZO framework and then dried in an argon-filled glovebox for 24 h. Finally, in order to obtain LLISE, autoclaving at 80 °C for 10 min was required. Here, the concentration of LLZO nanosheets was utilized to control the thickness of LLISE. LLISE- x (x = thickness, μm) represents the LLISE with different thicknesses. In order to obtain LN/PEO CSEs with a thickness of 140 μm , a PEO-LiTFSI-acetonitrile solution (EO/Li molar ratio of 18:1) was first prepared, and LLZO nanosheets with different contents were added into above solution. Next, the mixed solution was stirred at room temperature for 10 h, and then, it was cast on a polytetrafluoroethylene (PTFE) plate and finally dried under an argon atmosphere at normal pressure and 40 °C for 12 h, followed by dried at 55 °C under vacuum for 12 h. It is worth noting that the above operations were all carried out in a glovebox filled with argon gas.

LLZO nanosheets were synthesized using two-step sintering manner and subsequently liquid-phase exfoliation. It can be seen from the AFM images (Fig. 7.38a) that LLZO nanosheets are about 4.5 nm thick and have lateral dimension of 3–5 μm . In order to verify the good crystallinity of the LLZO nanosheets, high-magnification TEM image (Fig. 7.38b) was taken, and the results show that the nanosheets have clearer and more ordered lattice fringes [97]. These results confirm the successful preparation of LLZO nanosheets.

Figure 7.39 shows the preparation process of LLISE. In order to obtain the layered LLZO framework, vacuum filtration is employed to assemble the resultant LLZO nanosheets into a film, followed by dispersing the solution on a nylon substrate and vacuum filtration to facilitate its film formation. It is worth noting that in order to obtain uniform and defect-free stacking of LLZO nanosheets on the base membrane, it is necessary to employ a low-pressure and uniform suction filtration. Then, the small amount of PEO-LiTFSI-acetonitrile solution was drawn into the interlayer by

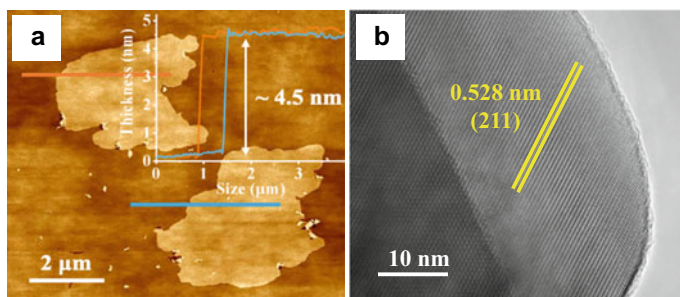


Fig. 7.38 **a** AFM image of LLZO nanosheets with corresponding height profiles and **b** high-magnification TEM image of LLZO nanosheets. Copyright (2022), Elsevier [31]

utilizing the layered structure of the LLZO framework, which was dried in an argon-filled glovebox for one day to obtain LLISE. In the above operation, it is necessary to ensure that the acetonitrile in the structure is completely removed. In the end, in order to improve the interlayer contact and obtain a denser film, hot pressing at 80 °C is utilized. PEO plays three main roles in LLISE: (1) It acts as a binder to improve the mechanical properties of the electrolyte; (2) the presence of PEO makes the surface of the garnet electrolyte smoother and improves the contact between the separator and the positive electrode and the lithium metal negative electrode [98]; and (3) it provides necessary sites for the transfer of lithium ions between layers. LLISE surface is smoother than that of the layered framework as shown by SEM image in Fig. 7.40a. The thickness of the LLISE is about 20 μm (Fig. 7.40b) as revealed by the cross-sectional SEM image. Different thicknesses of LLISEs were prepared to study the effect of thickness on lithium-ion migration, and the thinnest LLISE can reach 12 μm .

Ionic conductivity is an important reference to measure the quality of electrolytes. A comparison of LN/PEO CSE (140 μm) and LLZO particles (200 μm) highlights

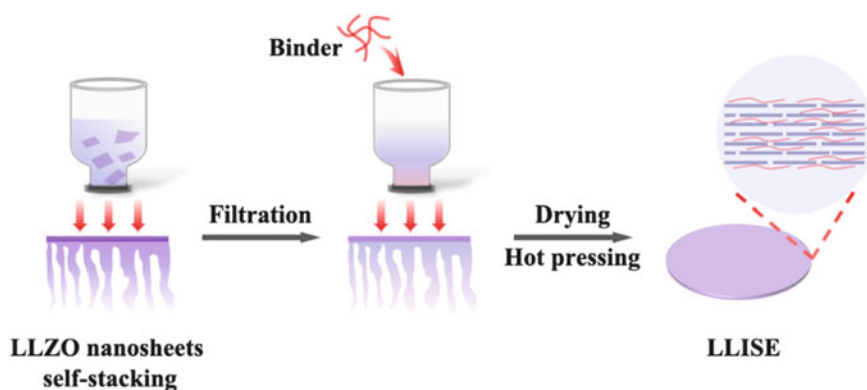


Fig. 7.39 Flowchart for the preparation of LLISE. Copyright (2022), Elsevier [31]

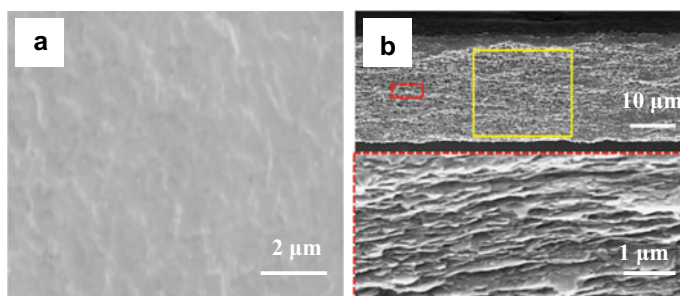


Fig. 7.40 a Surface SEM images of LLISE. b Cross-sectional SEM images of LLISE at different magnifications. Copyright (2022), Elsevier [31]

the strengths of LLISE as a framework material. The ionic conductivity of LN/PEO CSE at 25 °C is $1.61 \times 10^{-5} \text{ S cm}^{-1}$ while the ionic conductivity of LLZO pellet at 25 °C is $1.02 \times 10^{-5} \text{ S cm}^{-1}$. By comparison, it can be seen that the ionic conductivity of LLISE-12 at 25 °C is $1.04 \times 10^{-4} \text{ S cm}^{-1}$, which is 5.5 times and 9.2 times higher than that of LN/PEO CSE and LLZO pellet, respectively. The continuous transport path, low grain boundary resistance, and short diffusion distance of LLZO enable its Li-ion conductivity [45, 94, 99]. At the same time, in Fig. 7.41a, the Arrhenius ionic conductivity plots of as-prepared electrolytes are conducted. Comparing with LN/PEO CSE, LLISE-12 and LLZO pellet electrolytes show no significant change in transfer activation energy (E_a) below and above the melting temperature of PEO. The above phenomena suggest that the lithium-ion transfer in LLISE-12 and LLZO pellet is dominated by the LLZO phase, and a small amount of PEO in the LLISE interlayer does not significantly alter the performance of LLZO [18]. LLISE-12 possesses a low Li-ion transfer activation energy (0.36 eV), much lower than that of LN/PEO CSE (1.22 eV), due to the continuous LLZO transfer pathways. However, as for LLZO pellet, although the LLZO phase is continuous, its E_a (0.38 eV) is higher than that of LLISE-12. This should be attributed to the fact that LLZO pellet has large grain boundary resistance and thick film thickness. As shown in Fig. 7.41b, grain boundary resistance measurements of LLISE-12 and LLZO pellet were performed in the frequency range from 1 MHz to 0.1 Hz. The grain boundary resistance of LLZO particles is calculated to be $1847.5 \Omega \text{ cm}^2$ by the equivalent circuit calculation, which is related to the semicircle and grain boundary resistance at high frequencies. In contrast, LLISE-12 has a weaker grain boundary capacitive reactance signal due to its low grain boundary resistance, so no obvious semicircle is observed [100]. LLISEs with different thicknesses were prepared, and the ionic conductivity of each thickness is measured to show the effect of thickness on Li-ion conductivity (Fig. 7.41c). The ionic conductivities of LLISEs with the thicknesses of 140, 60, and 20 μm at 25 °C are 2.53×10^{-5} , 5.71×10^{-5} , and $8.48 \times 10^{-5} \text{ S cm}^{-1}$, respectively. When the thickness of LLISE changes from 12 μm to 140 μm , the ionic conductivity is dropped by 76%. The above data indicate that thin electrolyte has superior ionic conductivity [101, 102]. This is because the short diffusion distance of lithium ions and the reduction of grain boundary resistance can significantly improve the ionic conductivity.

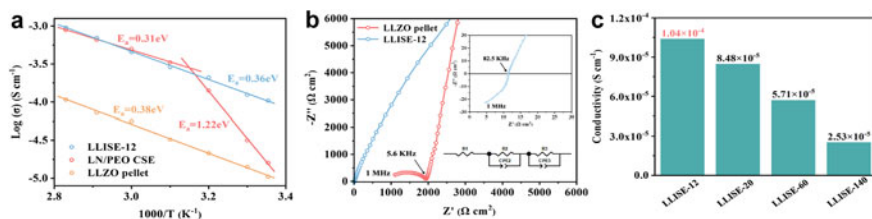


Fig. 7.41 a The ionic conductivities of LLZO pellet, LN/PEO CSE, and LLISE-12. b EIS of LLISE-12 and LLZO pellet with frequency ranging from 1 MHz to 0.1 Hz at 25 °C. c The ionic conductivities of LLISE-140, LLISE-60, LLISE-20, and LLISE-12. Copyright (2022), Elsevier [31]

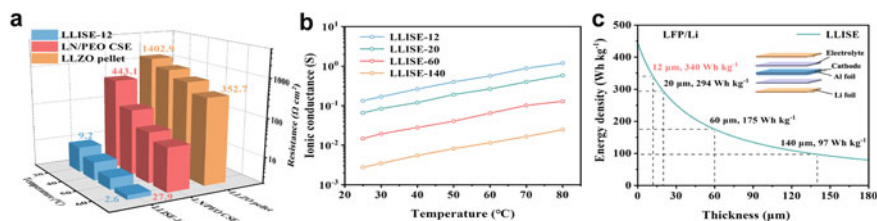


Fig. 7.42 a The temperature-dependent ASR of LLZO pellet, LN/PEO CSE, and LLISE-12. b The temperature-dependent ionic conductances of LLISE-140, LLISE-60, LLISE-20, and LLISE-12. c Gravimetric energy density as a function of thickness of LLISE employing LFP cathode (inset shows an idea pouch cell model). Copyright (2022), Elsevier [31]

Area-specific resistance (ASR) is an effective parameter to measure the internal resistance of the cell [103, 104]. The ASR value of LN/PEO CSE is $443.1 \Omega \text{ cm}^2$ at 30°C , while it of LLZO particles is $1402.9 \Omega \text{ cm}^2$ at 30°C (Fig. 7.42a). At 30°C , the LLISE-12 achieves an ultra-low ASR ($9.2 \Omega \text{ cm}^2$), which is more than 150 times lower than that of LLZO pellet, mainly due to its thin thickness and high ionic conductivity. Due to the different thickness of each electrolyte, the ionic conductance becomes a more direct measure of the energy density of ASSLBs [101, 103]. The corresponding ionic conductances of LLISE at different thicknesses are shown in Fig. 7.42b. Among them, the highest ionic conductance of LLISE-12 at 30°C is 0.17 S, which is twice that of LLISE-20, 9 times of that of LLISE-60, and 48 times of that of LLISE-140. Shorter lithium-ion diffusion distance and reduced grain boundary resistance help the realization of such high ionic conductance. Figure 7.42c shows the idea of pouch cell model calculation of LLISE gravimetric energy density, which provides guidance for the design of ASSLBs. The gravimetric energy density of LLISE-12 can reach 340 Wh kg^{-1} when the electrolyte thickness is $12 \mu\text{m}$. It is worth noting that when compared with other types of electrolytes, the combined performance of LLISE is better in both ionic conductance and energy density.

In order to evaluate the stability of the as-prepared SSE in lithium stripping and electroplating reactions, lithium symmetric batteries were assembled. The cycling test was performed at 0.2 mA cm^{-2} at 60°C . The choice of LLISE-20 to assemble the battery is because of its better overall performance. The LN/PEO CSE is shorted after 184 h as shown in Fig. 7.43a. By comparison, it can be seen that LLISE-20 has better cycling stability, the cycling time is as long as 1500 h, and the overpotential is as low as about 28 mV. The long-term cycling stability of LLISE-20 is due to its good mechanical strength and high electrical conductivity, which enables uniform deposition of Li ions at the interface [45]. According to the SEM image, it can be seen that a large number of irregular lithium dendrites appear on the surface of the lithium electrode cycled in the LN/PEO CSE. Conversely, as shown in Fig. 7.43b, c, the Li sheet surface of the Li/LLISE-20/Li symmetric cell is smooth and defect-free. The above experimental results indicate a high ionic conductivity of LLISE-20 due to its short diffusion distance, continuous transport path, and low grain boundary

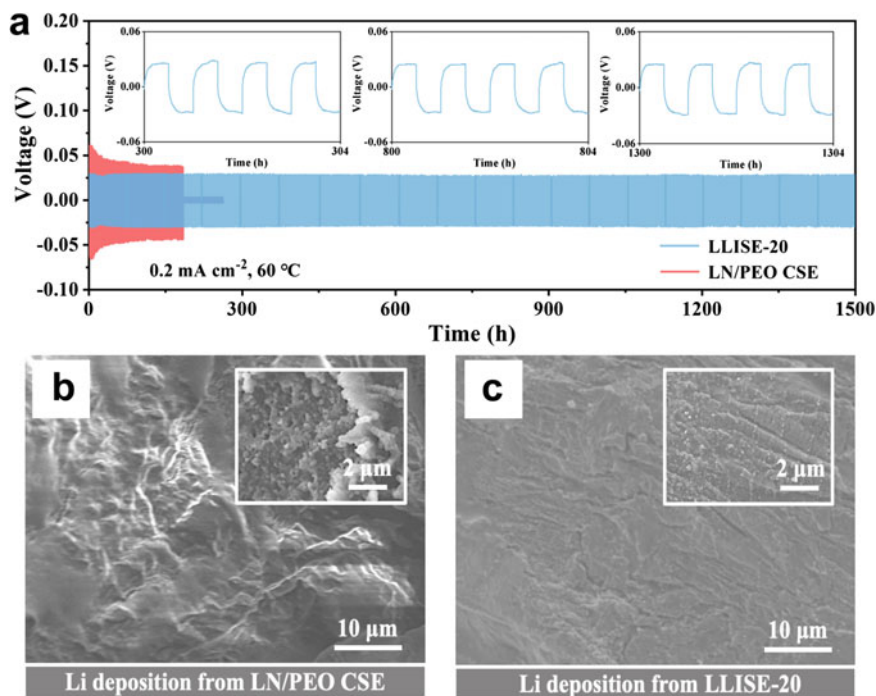


Fig. 7.43 **a** Long-term cycling of Li/LN/PEO CSE/Li and Li/LLISE-20/Li cells at 60 °C (inset shows voltage profiles of Li/LLISE-20/Li at 300, 800, and 1300 h, respectively). **b** and **c** Surface SEM images of Li cathode after lithium plating/stripping in Li/LN/PEO CSE/Li and Li/LLISE-20/Li cells (inset reveals zoomed-in SEM images). Copyright (2022), Elsevier [31]

resistance of LLZO, thus enabling uniform deposition of Li ions at the interface. Finally, this affords high Li-ion migration number (0.91) to LLISE-20 [105].

In order to test the mechanical strength of LN/PEO CSE, PEO/LiTFSI, and LLISE electrolytes and verify the ability of SSEs in inhibiting the growth of lithium dendrites, nanoindentation technology was selected to simulate the growth of lithium dendrites [15]. The compressive strength of LLISE-20 is 3.2 GPa, which is about 10 times higher than that of LN/PEO CSE, as shown in Fig. 7.44a, b. It is worth noting that PEO is easily penetrated by the indenter because the maximum loading force applied in the nanoindentation test is only 3 mN. Therefore, the layered framework formed by LLZO nanosheets enhances the compressive strength of LLISE-20.

Long-cycling and rate performance tests were performed by assembling the LFP/SSE/Li cells. As shown in Fig. 7.45a, they are the cycling performances of the battery at 0.5C at 60 °C. Among them, the battery assembled with LLISE-20 has better cycling performance, while the LFP/LN/PEO CSE/Li battery-assembled battery has a sharp capacity decline after 92 cycles. The battery assembled with LLISE-20 remains stable after 200 cycles, and the capacity decay per cycle is not higher than 0.05%. Its initial discharge capacity is 164.2 mAh g⁻¹, and its Coulombic

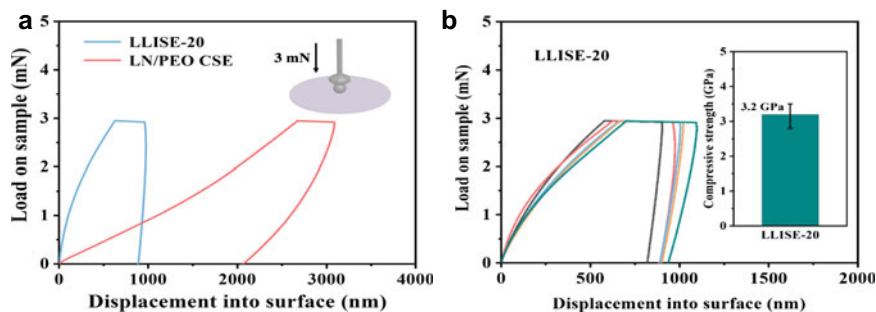


Fig. 7.44 **a** Load–displacement curves of LN/PEO CSE and LLISE-20 under nanoindentation test. **b** Load–displacement curves of LLISE-20 under nanoindentation test (inset displays the error bar of compressive strength). Copyright (2022), Elsevier [31]

efficiency is close to 100% after long-term cycling charge–discharge. By comparing the cycling performance of LFP/LLISE-20/Li battery and LN/PEO CSE battery at 60 °C at 0.5C, it can be seen that the electrochemical performance of LLISE-20 is relatively stable, as shown in Fig. 7.45b. From the above results, the excellent long-cycle performance of the LFP/LLISE-20/Li full cell should be attributed to the short and continuous transport path of LLZO, which results in its high ionic conductivity and good physicochemical stability. In addition, after 150 cycles, the LFP/LLISE-20/Li battery exhibits a Coulombic efficiency of 95.2% and a discharge capacity of 142.2 mAh g⁻¹. The above cycling data is measured at a lower operating temperature of 45 °C, and a plateau of low polarization voltage can be observed as shown in Fig. 7.45c, d. The excellent cycle performance of LFP/LLISE-20/Li cell can be further confirmed by the above data.

The rate performance of the cell is shown in Fig. 7.46a. The LFP/LLISE-20/Li cell provides high discharge capacity of 164.2, 161.4, 158.7, 148.2, and 123.5 mAh g⁻¹ when cycling at 0.1, 0.2, 0.4, 0.6, and 1.0C, respectively. However, the discharge capacity of the LN/PEO CSE battery decreases significantly from 0.6C to 1.0C. LFP/LLISE-20/Li cell displays an excellent cycling performance with a discharge capacity of 162.8 mAh g⁻¹, and 99.1% of initial capacity was maintained when the rate returns to 0.1C. The voltage curves at different rates show that LFP/LLISE-20/Li obtains a plateau with low polarization voltage as shown in Fig. 7.46b. The above experimental data show that LLISE-20 has good contact with the electrode interface, high ionic conductivity, and stable physical and chemical properties, which lead to the superior rate performance for LFP/LLISE-20/Li battery. The above experimental phenomena also indicate that the layered ISE in ASSLB has great potential for practical application.

In conclusion, LLZO nanosheets with a thickness of about 4.5 nm and lateral dimensions of 3–5 μm were successfully fabricated, and on this basis, thin (12 μm) and defect-free LLISEs were fabricated. The high ionic conductivity of LLISE is due to the low grain boundary resistance, short diffusion distance, and continuous transport path of LLZO. The ionic conductivity of LLISE at 30 °C is 1.30 × 10⁻⁴ S

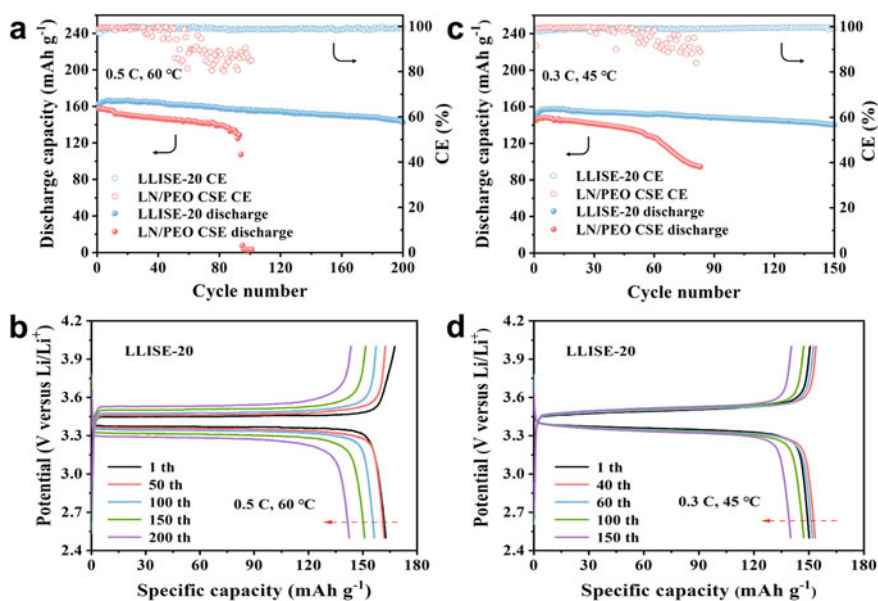


Fig. 7.45 All-solid-state LFP/Li battery performances. **a** Cycling performances of the cells assembled with different electrolytes at 60 °C under 0.5C. **b** Charge–discharge profiles of LFP/LLISE-20/Li cell at 60 °C under 0.5C. **c** Cycling performances of the cells assembled with different electrolytes at 45 °C under 0.3C. **d** Charge–discharge profiles of LFP/LLISE-20/Li cell at 45 °C under 0.3C. Copyright (2022), Elsevier [31]

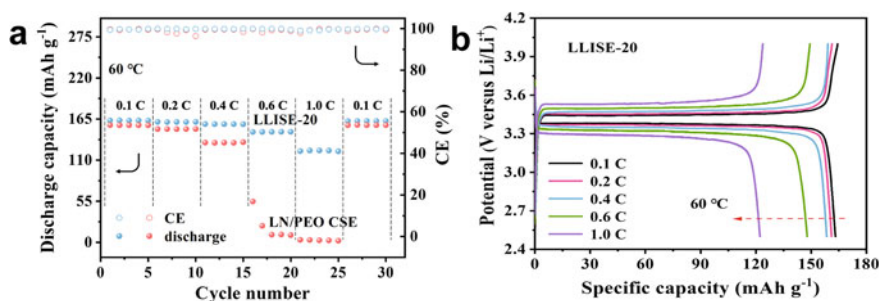


Fig. 7.46 All-solid-state LFP/Li cell performances. **a** Rate performances of the cells assembled with different electrolytes at 60 °C under different rates. **b** Charge–discharge profiles of LFP/LLISE-20/Li cell at 60 °C under different rates. Copyright (2022), Elsevier [31]

cm⁻¹, which is an order of magnitude higher than that of LLZO pellets (>200 μm) prepared by cold pressing. Notably, compared to most reported SSEs, LLISE has high ionic conductivity (0.17 S) and high-energy density of 340 Wh kg⁻¹ at 30 °C due to its thin thickness. At the same time, the compressive strength of LLISE is as high as 3.2 GPa when its thickness is 20 μm. The assembled Li/LLISE/Li cell

can cycle stably over 1500 h with a low polarization under 0.2 mA cm^{-2} and $60 \text{ }^\circ\text{C}$. Furthermore, the LFP/LLISE/Li cell displays an excellent cycling performance with a discharge capacity of 143 mAh g^{-1} after 200 cycles with low capacity decay of 0.05% per cycle at 0.5C and $60 \text{ }^\circ\text{C}$. High-performance SSEs can be fabricated through the self-stacking of ISE nanosheets, which hold promise for the development of advanced solid-state electrolytes.

7.7 Laminar LLTO/Vr Composite Electrolyte

Vermiculite (Vr) nanosheets were prepared using two-step ion exchange method [106]. Laminar LLTO/Vr composite electrolytes (Vr-LLTO LISE) were fabricated by a method that consists of swelling filtration and sintering, as shown in Fig. 7.47. Firstly, Vr laminar framework was obtained by filtrating the Vr nanosheets. Subsequently, the Vr laminar framework was swelled in ethanol to get a larger inter-layer spacing. Then, precursor solution was prepared by solving the inorganic salt ($(\text{NO}_3)_3 \cdot 6\text{H}_2\text{O}$, $\text{Ti}(\text{OC}_4\text{H}_9)_4$, and LiNO_3) with certain concentration in the mixture solution of anhydrous ethanol and acetic acid (volume ratio of 8:2), which was filtrated into Vr laminar framework. Afterward, Vr-LLTO LISE was obtained for drying at $60 \text{ }^\circ\text{C}$ for 3 h, sintering for 2 h at $1000 \text{ }^\circ\text{C}$, and then annealing. LLTO nanoparticles were obtained by the sol-gel method [30]. For the preparation of LLTO pellet, the LLTO nanoparticles were hot-pressed in a graphite die at $1000 \text{ }^\circ\text{C}$ with a pressure of 40 MPa for 2 h in argon atmosphere. To enhance the interface contact between electrolyte and electrodes, a thin layer of PEO-LiTFSI (EO: $\text{Li}^+ = 16:1$) was coated on the electrolyte surface and then dried at $50 \text{ }^\circ\text{C}$. Next, a slight pressure was employed to promote the interface contact at $80 \text{ }^\circ\text{C}$ [99].

Vr laminar framework was obtained by filtrating Vr nanosheets. Constant-rate and low-pressure filtration manner were employed to help rigid Vr nanosheets building ordered laminar framework. Subsequently, hydrophilic Vr laminar framework was swollen in low-concentration precursors, and the vacuum filtration process is to let

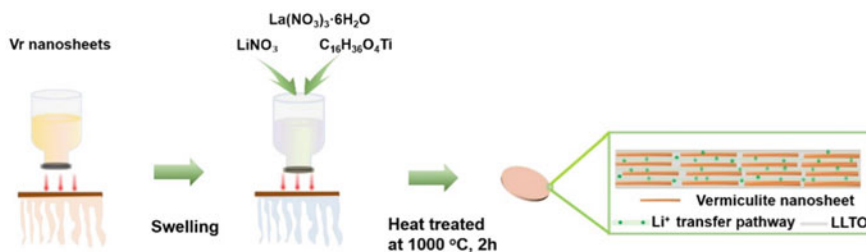


Fig. 7.47 Synthetic diagram of Vr-LLTO LISE preparation. Copyright (2021), John Wiley and Sons [32]

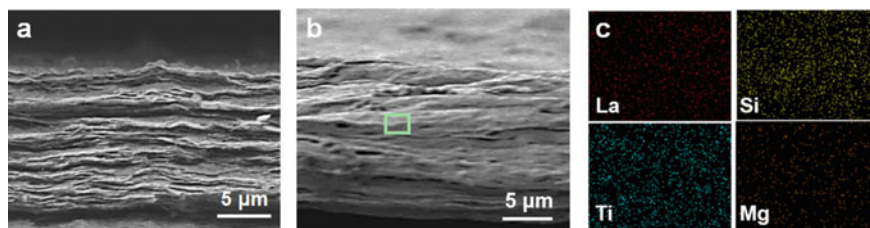


Fig. 7.48 Cross-sectional SEM image of **a** Vr laminar framework and **b** Vr-LLTO LISE. **c** Cross-sectional SEM image of Vr-LLTO LISE corresponding EDS mappings of La, Si, Ti, and Mg elements. Copyright (2021), John Wiley and Sons [32]

precursors continuously and uniformly distribute in interlayer channels. Finally, Vr-LLTO LISE was obtained by annealing and traditional sintering process. As shown in Fig. 7.48a, b, the thickness of Vr-LLTO LISE increases from 13 to 15 μm , due to the growth of LLTO crystals in interlayer channels. La, Si, Ti, and Mg elements are uniformly dispersed throughout the Vr-LLTO LISE, which indicates that the LLTO crystals are uniformly distributed in the interlayer channels (Fig. 7.48c).

Then, the arrangement and morphology of LLTO crystals in Vr-LLTO LISE are explored. TEM images display that the Vr-LLTO LISE has an ordered 2D laminar structure, where the bright and dark areas correspond to the LLTO crystal and Vr nanosheet, respectively (Fig. 7.49a). Importantly, under high-resolution TEM images, the LLTO crystals have no detectable void and structural defect, implying that the LLTO crystals are continuously arranged in the interlayer channels. Besides, the distance is 0.274 nm between adjacent fringes (Fig. 7.49b). This corresponds to LLTO crystal (110) plane, which means that LLTO crystal preferentially grows along the [001] direction (i.e., *c*-axis) in interlayer channels. Moreover, in LLTO crystal, the fastest direction for Li^+ transfer is the *c*-axis due to the large number of vacancies in La-poor layer [107, 108]. In contrast, LLTO crystal grown in open spacing shows obvious defects due to the infinite growth in different directions. However, as shown in Fig. 7.49c, there are various crystal planes [e.g., (101), (110), and (001)] in LLTO nanoparticles. In general, these findings indicate that the 2D channel confinement effect promotes the ordered arrangement and growth of LLTO crystals, thereby reducing structural defects.

In confined 2D channels, the exploration of LLTO crystal growth mechanism is also important. To this end, another two laminar frameworks composed of rigid, hydrophobic $\text{g-C}_3\text{N}_4$ and flexible, hydrophilic GO, were also manufactured for crystal growth. In Fig. 7.50a, XRD results show that the (001)/(110) peak intensity ratio of LLTO crystal is 13.7% when growing in open spacing. In contrast, the proportions of LLTO crystals grown in the Vr, GO, and $\text{g-C}_3\text{N}_4$ laminar frameworks are 9.8%, 12.9%, and 13.4%, respectively. It can be seen that the peak intensity ratio decreases, which means that when growing in confined spacing, LLTO crystals preferentially grow along the *c*-axis, and the proportion of (001) crystal plane perpendicular to *c*-axis is decreased [109, 110]. LLTO crystals grown in laminar frameworks

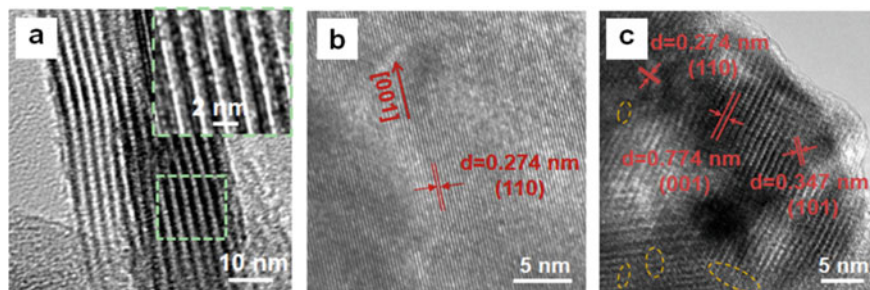


Fig. 7.49 **a** High-magnification TEM images of Vr-LLTO LISE cross-sectional. **b** High-resolution TEM images of surface slice of Vr-LLTO LISE. **c** High-resolution TEM images of LLTO nanoparticle (yellow circles areas are structural defects). Copyright (2021), John Wiley and Sons [32]

composed of rigid and hydrophilic Vr nanosheets have the lowest (001)/(110) peak intensity ratio, which means that hydrophilicity and rigidity are important for uniform and prior growth of LLTO crystals in 2D channels. The Raman peaks in Fig. 7.50c show that the peak of LLTO pellet at 146.8 cm^{-1} corresponds to vibration of Ti–O bond in the *a-b* plane, and the peak at 553.4 cm^{-1} corresponds to the vibration of Ti–O bond on the *c*-axis of Ti-O_6 [111]. In the spectrum of Vr-LLTO LISE, the corresponding peaks red-shift to 140.9 cm^{-1} and blue-shift to 572.4 cm^{-1} , respectively. In confined interlayer channel, the growth of LLTO crystals along *a*-axis and *b*-axis is limited, while the growth of LLTO crystals along *c*-axis is almost unaffected. As shown in Fig. 7.50b, 2D wide-angle XRD results provide further evidence. Compared to LLTO pellet, the (101) crystal plane of Vr-LLTO LISE displays a brighter ring, which means that more (101) crystal planes are formed along the *c*-axis.

As depicted In Fig. 7.51c, the ionic conductivity of LLTO pellet is close to the data in the literature, which is $1.77 \times 10^{-5} \text{ S cm}^{-1}$ at $30 \text{ }^\circ\text{C}$ [112]. In contrast, the ionic conductivity of Vr-LLTO LISE reaches $8.22 \times 10^{-5} \text{ S cm}^{-1}$ at $30 \text{ }^\circ\text{C}$, which is 364% higher than that of LLTO pellet. The increase in ionic conductivity is

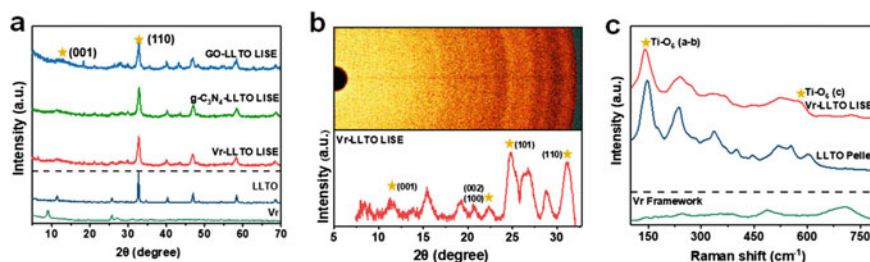


Fig. 7.50 **a** XRD patterns of GO-LLTO LISE, $\text{g-C}_3\text{N}_4$ -LLTO LISE, Vr-LLTO LISE, LLTO, and Vr laminar framework. **b** 2D wide-angle X-ray diffraction patterns of Vr-LLTO LISE. **c** Raman spectra of Vr laminar framework, LLTO pellet, and Vr-LLTO LISE. Copyright (2021), John Wiley and Sons [32]

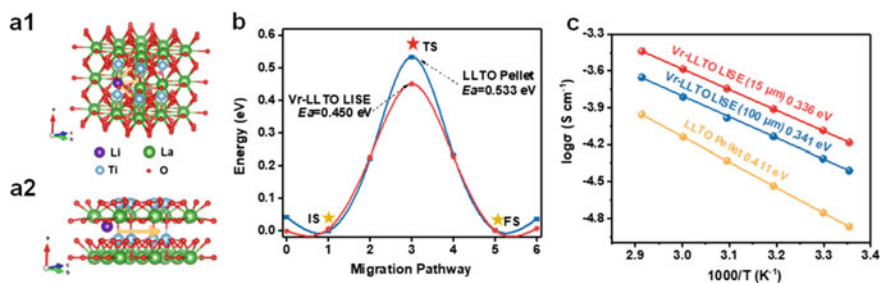


Fig. 7.51 **a1** Li^+ transport diagram in 3D LLTO crystal. **a2** Li^+ transport diagram in 2D LLTO crystal. **b** Energy profiles of the Li^+ transport pathways in LLTO pellet and Vr-LLTO LISE. **c** Conductivity of LLTO pellet and Vr-LLTO LISE with thicknesses of 15 and 100 μm , respectively. Copyright (2021), John Wiley and Sons [32]

owing to the ordered arrangement of LLTO crystals, which reduce inherent structural defects and lower grain boundary resistance. The activation energies of LLTO pellet (0.411 eV) and Vr-LLTO LISE (0.336 eV) provides direct evidence, which is close to grain boundary and bulk activation energies, respectively [16]. This indicates that the main transport mechanism in Vr-LLTO LISE is similar to the bulk Li^+ transfer of LLTO, which highlights the advantages of LLTO crystal grown in confined spacing. LLTO pellet and Vr-LLTO LISE with the same thickness (100 μm) were prepared for comparison. As LLTO crystals are orderly arranged in the electrolyte, the thicker Vr-LLTO LISE gains a low activation energy value (0.341 eV).

Further, Li^+ transport mechanism was investigated in Vr-LLTO LISE using density functional theory (DFT) simulations. Li^+ transport energy barrier was calculated. Fig. 7.51a1 is a geometric model of 3D LLTO crystals grown in open space, and 2D LLTO crystals grown in confined spacing are shown in Fig. 7.51a2. In LLTO crystals, the La-poor layer and La-rich layer are alternately stacked. For 2D LLTO crystals grown in confined spacing, the ordered and large-size crystals along the c -axis act as the fast transport channel of Li^+ . However, due to the existence of different crystal planes, the transport direction of Li^+ in 3D LLTO crystals is random. As shown in Fig. 7.51b, the transport energy distributions in the 2D and 3D LLTO crystals prove this statement. The energy barriers of 2D and 3D LLTO crystal are 0.450 eV and 0.553 eV, respectively. This proved that the energy barrier of Li^+ passing through the c -axis is lower than that passing through the a -axis and b -axis, and the transport of Li^+ is mainly along c -axis in the 2D LLTO crystal.

Vr-LLTO LISE displays excellent mechanical stability. As shown in Fig. 7.52a, the lithium dendrite growth process was simulated by nanoindentation test to evaluate the Vr-LLTO LISE mechanical stability. A good compressive modulus of 1.24 GPa is obtained for Vr-LLTO LISE with the thickness of only 15 μm . Furthermore, the final depth and maximal displacement after unloading of the Vr-LLTO LISE reach 748 and 1120 nm, respectively, higher than those of LLTO pellet (582 and 664 nm). This demonstrates that Vr-LLTO LISE has good flexibility. In Fig. 7.52b, the interlayer force was directly quantified using nanoscratch. The critical loading of Vr-LLTO

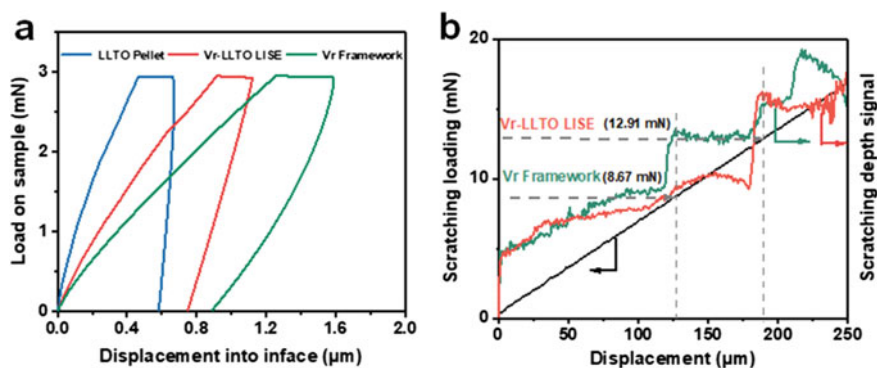


Fig. 7.52 **a** Under nanoindentation test, load–displacement curves of LLTO pellet, Vr-LLTO LISE, Vr laminar framework. **b** Nano crack results of Vr-LLTO LISE and Vr laminar framework. Copyright (2021), John Wiley and Sons [32]

LISE is 49% higher than that of Vr laminar framework (8.67 mN), indicating that the interlayer force is stronger.

As shown in Fig. 7.53, voltage profiles of the lithium stripping/plating behaviors at 60 °C in lithium symmetrical batteries were tested. It can be seen that at a current density of 0.2 mA cm⁻², the lithium symmetrical battery with LLTO pellet has a high overpotential of about 68 mV, coupled with a short circuit at 252 h. In contrast, the lithium symmetric battery with Vr-LLTO LISE can be stably cycled for over 1200 h with a low overpotential of about 50 mV. Then, in order to calculate the critical current densities, the symmetric batteries of LLTO pellet and Vr-LLTO LISE were measured.

LFP/Li batteries with LLTO pellet, Vr-LLTO LISE (15 μm), and Vr-LLTO LISE (100 μm) electrolytes were assembled and tested at 60 °C to evaluate the rate and cycling performances. LLTO pellet-assembled battery appears short circuit after 47

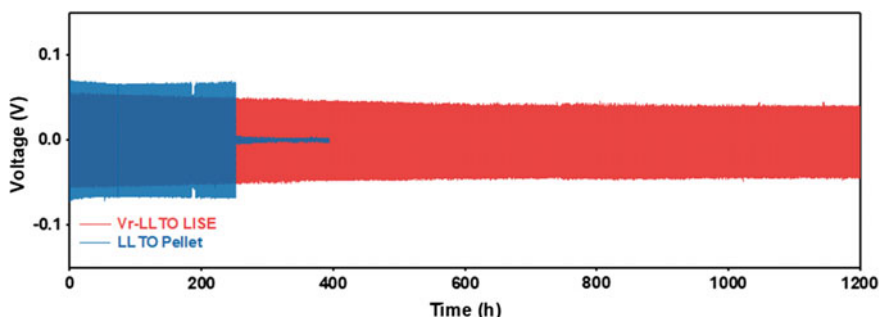


Fig. 7.53 LLTO pellet and Vr-LLTO LISE-assembled Li symmetric batteries cycling performance under 0.2 mA cm⁻² at 60 °C. Copyright (2021), John Wiley and Sons [32]

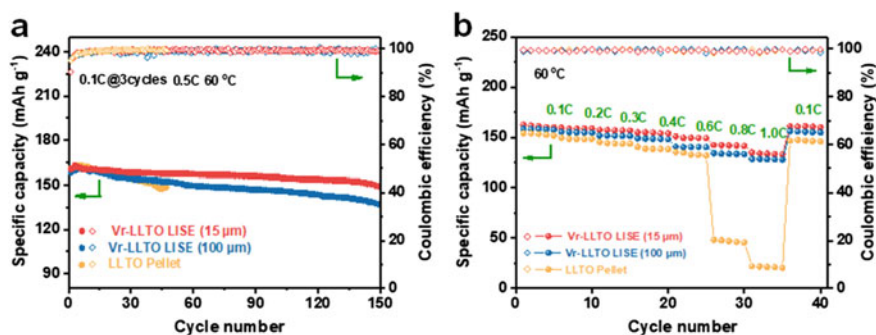


Fig. 7.54 **a** Cycling performances (0.1C in the first three cycles and 0.5C in the latter cycles) and **b** rate performances of different batteries assembled with LLTO pellet and 15 μm- and 100 μm-thick Vr-LLTO LISE at 60 °C. Copyright (2021), John Wiley and Sons [32]

cycles due to serious structural defects (Fig. 7.54a). In contrast, the discharge capacities of 15 μm- and 100 μm-thick Vr-LLTO LISEs reach 148.9 and 137 mAh g⁻¹ after 150 cycles, respectively. The battery assembled with Vr-LLTO LISE with 15 μm thickness shows only 0.057% capacity reduction per cycle, proving its excellent cycling performance. The LFP/Vr-LLTO LISE (15 μm)/Li batteries operated at 60 °C exhibit discharge capacities of 162.3, 158.7, 156.8, 153.9, 149.7, 140.3, and 131.5 mAh g⁻¹ at 0.1, 0.2, 0.3, 0.4, 0.6, 0.8, and 1.0C, respectively (Fig. 7.54b). And a capacity of 159.8 mAh g⁻¹ could be recovered when the rate resets to 0.1C, showing good cycling stability and reversibility. Overall, the excellent rate and cycling performances demonstrate Vr-LLTO LISE has great application in ASSLBs.

In conclusion, we report the preparation of defect-free, oriented, and large-size 2D LLTO crystal, through controlling the arrangement and growth of crystal in confined spacing. Due to the ordered arrangement of LLTO crystals, the structural defects are efficiently eliminated, endowing Vr-LLTO LISE with ultrafast Li⁺ transport. At 30 °C, the synthesized Vr-LLTO LISE with a thickness of 15 μm exhibits a high ionic conductance of 87.2 mS and high ionic conductivity of 8.22×10^{-5} S cm⁻¹, outperforming most reported LLTO-based electrolytes. Furthermore, the Vr lamina framework with linking by covalent bonds exhibits good toughness, which provides excellent mechanical properties for Vr-LLTO LISE. Under 0.5C at 60 °C, the assembled LFP/Li battery can still achieve a high capacity of 148.9 mAh g⁻¹ after 150 cycles and the capacity decay of each cycle is only 0.057%, showing excellent cycling stability. Theoretical calculation and experimental results show that the transfer and growth mechanisms of LLTO crystals in confined spacing are established. The 2D confinement effect of hydrophilic and rigid channel enables the long-range, ordered arrangement of LLTO crystals along *c*-axis, which then eliminate structural defects, construct a fast Li⁺ transfer path, and promote Li⁺ conduction. The 2D LLTO crystal with controlled arrangement and growth of LLTO crystals in confined spacing provides a promising method for design of ultrafast Li⁺ transfer devices.

References

1. D. Lin, Y. Liu, Y. Cui, Reviving the lithium metal anode for high-energy batteries. *Nat. Nanotechnol.* **12**, 194–206 (2017)
2. A. Manthiram, X. Yu, S. Wang, Lithium battery chemistries enabled by solid-state electrolytes. *Nat. Rev. Mater.* **2**, 16103 (2017)
3. S. Xia, X. Wu, Z. Zhang, Y. Cui, W. Liu, Practical challenges and future perspectives of all-solid-state lithium-metal batteries. *Chemistry* **5**, 753–785 (2019)
4. D. Zhou, D. Shanmukaraj, A. Tkacheva, M. Armand, G. Wang, Polymer electrolytes for lithium-based batteries: advances and prospects. *Chemistry* **5**, 2326–2352 (2019)
5. L. Xu, J. Li, W. Deng, H. Shuai, S. Li, Z. Xu, J. Li, H. Hou, H. Peng, G. Zou, X. Ji, Garnet solid electrolyte for advanced all-solid-state Li batteries. *Adv. Energy Mater.* **11**, 2000648 (2020)
6. J.W. Fergus, Ceramic and polymeric solid electrolytes for lithium-ion batteries. *J. Power Sour.* **195**, 4554–4569 (2010)
7. F. Lv, Z. Wang, L. Shi, J. Zhu, K. Edström, J. Mindemark, S. Yuan, Challenges and development of composite solid-state electrolytes for high-performance lithium ion batteries. *J. Power Sour.* **441**, 227175 (2019)
8. E. Bakangura, L. Wu, L. Ge, Z. Yang, T. Xu, Progress in polymer science mixed matrix proton exchange membranes for fuel cells: state of the art and perspectives. *Prog. Polym. Sci.* **57**, 103–152 (2016)
9. Y. Li, G. He, S. Wang, S. Yu, F. Pan, H. Wu, Z. Jiang, Recent advances in the fabrication of advanced composite membranes. *J. Mater. Chem. A* **35**, 10058–10077 (2013)
10. L. Chen, W. Li, L.Z. Fan, C.W. Nan, Q. Zhang, Intercalated electrolyte with high transference number for dendrite-free solid-state lithium batteries. *Adv. Func. Mater.* **29**, 1901047 (2019)
11. Z. Zhang, R.G. Antonio, K.L. Choy, Boron nitride enhanced polymer/salt hybrid electrolytes for all-solid-state lithium ion batteries. *J. Power Sour.* **435**, 226736 (2019)
12. Y.S. Ye, H. Wang, S.G. Bi, Y. Xue, Z.G. Xue, X.P. Zhou, X.L. Xie, Y.W. Mai, High performance composite polymer electrolytes using polymeric ionic liquid-functionalized graphene molecular brushes. *J. Mater. Chem. A* **3**, 18064–18073 (2015)
13. Q. Pan, Y. Zheng, S. Kota, W. Huang, S. Wang, H. Qi, S. Kim, Y. Tu, M.W. Barsoum, C.Y. Li, 2D MXene-containing polymer electrolytes for all-solid-state lithium metal batteries. *Nanoscale Adv.* **1**, 395–402 (2019)
14. W. Liu, S.W. Lee, D. Lin, F. Shi, S. Wang, A.D. Sendek, Y. Cui, Enhancing ionic conductivity in composite polymer electrolytes with well-aligned ceramic nanowires. *Nat. Energy* **2**, 17035 (2017)
15. W. Tang, S. Tang, C. Zhang, Q. Ma, Q. Xiang, Y.W. Yang, J. Luo, Simultaneously enhancing the thermal stability, mechanical modulus, and electrochemical performance of solid polymer electrolytes by incorporating 2D sheets. *Adv. Energy Mater.* **8**, 1800866 (2018)
16. Z. Jiang, H. Xie, S. Wang, X. Song, X. Yao, H. Wang, Perovskite membranes with vertically aligned microchannels for all-solid-state lithium batteries. *Adv. Energy Mater.* **8**, 1801433 (2018)
17. K. Fu, Y. Gong, G.T. Hitz, D.W. McOwen, Y. Li, S. Xu, Y. Wen, L. Zhang, C. Wang, G. Pastel, J. Dai, B. Liu, H. Xie, Y. Yao, E.D. Wachsman, L. Hu, Three-dimensional bilayer garnet solid electrolyte based high energy density lithium metal-sulfur batteries. *Energy Environ. Sci.* **10**, 1568–1575 (2017)
18. A. Li, X. Liao, H. Zhang, L. Shi, P. Wang, Q. Cheng, J. Borovilas, Z. Li, W. Huang, Z. Fu, M. Dontigny, K. Zaghib, K. Myers, X. Chuan, X. Chen, Y. Yang, Nacre-inspired composite electrolytes for load-bearing solid-state lithium-metal batteries. *Adv. Mater.* **32**, 1905517 (2020)
19. M.J. Palmer, S. Kalnaus, M.B. Dixit, A.S. Westover, K.B. Hatzell, N.J. Dudney, X.C. Chen, A three-dimensional interconnected polymer/ceramic composite as a thin film solid electrolyte. *Energy Storage Mater.* **26**, 242–249 (2020)

20. J. Ding, R. Xu, C. Yan, Y. Xiao, Y. Liang, H. Yuan, J. Huang, Integrated lithium metal anode protected by composite solid electrolyte film enables stable quasi-solid-state lithium metal batteries. *Chin. Chem. Lett.* **31**, 2339–2342 (2020)
21. W. Liu, N. Liu, J. Sun, P.C. Hsu, Y. Li, H.W. Lee, Y. Cui, Ionic conductivity enhancement of polymer electrolytes with ceramic nanowire fillers. *Nano Lett.* **15**, 2740–2745 (2015)
22. C. Gerbaldi, J.R. Nair, M.A. Kulandainathan, R.S. Kumar, C. Ferrara, P. Mustarelli, A.M. Stephan, Innovative high performing metal organic framework (MOF)-laden nanocomposite polymer electrolytes for all-solid-state lithium batteries. *J. Mater. Chem. A* **2**, 9948–9954 (2014)
23. K. Jeong, S. Park, G.Y. Jung, S.H. Kim, Y.H. Lee, S.K. Kwak, S.Y. Lee, Solvent-free, single lithium-ion conducting covalent organic frameworks. *J. Am. Chem. Soc.* **141**, 5880–5885 (2019)
24. J. Bae, Y. Li, F. Zhao, X. Zhou, Y. Ding, G. Yu, Designing 3D nanostructured garnet frameworks for enhancing ionic conductivity and flexibility in composite polymer electrolytes for lithium batteries. *Energy Storage Mater.* **15**, 46–52 (2018)
25. Y. Gong, K. Fu, S. Xu, J. Dai, T.R. Hamann, L. Zhang, G.T. Hitz, Z. Fu, Z. Ma, D.W. McOwen, X. Han, L. Hu, E.D. Wachsman, Lithium-ion conductive ceramic textile: a new architecture for flexible solid-state lithium metal batteries. *Mater. Today* **21**, 594–601 (2018)
26. S. Zekoll, C. Marriner-Edwards, A.K.O. Hekselman, J. Kasemchainan, C. Kuss, D.E.J. Armstrong, D. Cai, R.J. Wallace, F.H. Richter, J.H.J. Thijssen, P.G. Bruce, Hybrid electrolytes with 3D bicontinuous ordered ceramic and polymer microchannels for all-solid-state batteries. *Energy Environ. Sci.* **11**, 185–201 (2018)
27. Z. Yang, Z. Sun, C. Liu, Y. Li, G. Zhou, S. Zuo, J. Wang, W. Wu, Lithiated nanosheets hybridized solid polymer electrolyte to construct Li⁺ conduction highways for advanced all-solid-state lithium battery. *J. Power Sour.* **484**, 229287 (2021)
28. W. Kou, R. Lv, S. Zuo, Z. Yang, J. Huang, W. Wu, J. Wang, Hybridizing polymer electrolyte with poly(ethylene glycol) grafted polymer-like quantum dots for all-solid-state lithium batteries. *J. Membr. Sci.* **618**, 118702 (2021)
29. N. Peng, W. Kou, W. Wu, S. Guo, Y. Wang, J. Wang, Lamina composite solid electrolyte with poly(ethylene oxide)-threaded metal-organic framework nanosheets for high-performance all-solid-state lithium battery. *Energy Environ. Mater.* **0**, 1–10 (2021)
30. C. Liu, J. Wang, W. Kou, Z. Yang, P. Zhai, Y. Liu, W. Wu, J. Wang, A flexible, ion-conducting solid electrolyte with vertically bicontinuous transfer channels toward high performance all-solid-state lithium batteries. *Chem. Eng. J.* **404**, 126517 (2021)
31. S. Guo, W. Kou, W. Wu, R. Lv, Z. Yang, J. Wang, Thin lamina inorganic solid electrolyte with high ionic conductance towards high-performance all-solid-state lithium battery. *Chem. Eng. J.* **427**, 131948 (2022)
32. R. Lv, W. Kou, S. Guo, W. Wu, Y. Zhang, Y. Wang, J. Wang, Preparing two-dimensional ordered Li_{0.33}La_{0.557}TiO₃ crystal in interlayer channel of thin lamina inorganic solid-state electrolyte towards ultrafast Li⁺ transfer. *Angewandte Chemie International Edition*, **61**, e202114220 (2022)
33. D.C. Marcano, D.V. Kosynkin, J.M. Berlin, A. Sinitskii, Z. Sun, A. Slesarev, L.B. Alemany, W. Lu, J.M. Tour, Improved synthesis of graphene oxide. *ACS Nano* **4**, 4806–4814 (2010)
34. Y. He, J. Wang, H. Zhang, T. Zhang, B. Zhang, S. Cao, J. Liu, Polydopamine-modified graphene oxide nanocomposite membrane for proton exchange membrane fuel cell under anhydrous conditions. *J. Mater. Chem. A* **2**, 9548–9558 (2014)
35. Y. Liu, K. Ai, L. Lu, Polydopamine and its derivative materials: synthesis and promising applications in energy, environmental, and biomedical fields. *Chem. Rev.* **114**, 5057–5115 (2014)
36. J.H. Ryu, P.B. Messersmith, H. Lee, Polydopamine surface chemistry: a decade of discovery. *ACS Appl. Mater. Interfaces* **10**, 7523–7540 (2018)
37. S.M. Kang, S. Park, D. Kim, S.Y. Park, R.S. Ruoff, H. Lee, Simultaneous reduction and surface functionalization of graphene oxide by mussel-inspired chemistry. *Adv. Func. Mater.* **21**, 108–112 (2011)

38. Y.T. Weng, H.W. Liu, A. Pei, F.F. Shi, H. Wang, C.Y. Lin, S.S. Huang, L.Y. Su, J.P. Hsu, C.C. Fang, Y. Cui, N.L. Wu, An ultrathin ionomer interphase for high efficiency lithium anode in carbonate based electrolyte. *Nat. Commun.* **10**, 5824 (2019)
39. J. Shim, H.J. Kim, B.G. Kim, Y.S. Kim, D.G. Kim, J.C. Lee, 2D boron nitride nanoflakes as a multifunctional additive in gel polymer electrolytes for safe, long cycle life and high rate lithium metal batteries. *Energy Environ. Sci.* **10**, 1911–1916 (2017)
40. J. Wan, J. Xie, D.G. Mackanic, W. Burke, Z. Bao, Y. Cui, Status, promises, and challenges of nanocomposite solid-state electrolytes for safe and high performance lithium batteries. *Mater. Today Nano* **4**, 1–16 (2018)
41. B. Chen, Z. Huang, X. Chen, Y. Zhao, Q. Xu, P. Long, S. Chen, X. Xu, A new composite solid electrolyte PEO/Li₁₀GeP₂S₁₂/SN for all-solid-state lithium battery. *Electrochim. Acta* **210**, 905–914 (2016)
42. H. Chen, D. Adekoya, L. Hencz, J. Ma, S. Chen, C. Yan, H. Zhao, G. Cui, S. Zhang, Stable seamless interfaces and rapid ionic conductivity of Ca-CeO₂/LiTFSI/PEO composite electrolyte for high-rate and high-voltage all-solid-state battery. *Adv. Energy Mater.* **10**, 2000049 (2020)
43. X. Wang, Y. Zhang, X. Zhang, T. Liu, Y.H. Lin, L. Li, Y. Shen, C.W. Nan, Lithium-salt-rich PEO/Li_{0.3}La_{0.557}TiO₃ interpenetrating composite electrolyte with three-dimensional ceramic nano-backbone for all-solid-state lithium-ion batteries. *ACS Appl. Mater. Interfaces* **10**, 24791–24798 (2018)
44. Y. Lin, X. Wang, J. Liu, J.D. Miller, Natural halloysite nano-clay electrolyte for advanced all-solid-state lithium-sulfur batteries. *Nano Energy* **31**, 478–485 (2017)
45. J. Wu, Z. Rao, Z. Cheng, L. Yuan, Z. Li, Y. Huang, Ultrathin, flexible polymer electrolyte for cost-effective fabrication of all-solid-state lithium metal batteries. *Adv. Energy Mater.* **9**, 1902767 (2019)
46. D. Lin, P.Y. Yuen, Y. Liu, W. Liu, N. Liu, R.H. Dauskardt, Y. Cui, A silica-aerogel-reinforced composite polymer electrolyte with high ionic conductivity and high modulus. *Adv. Mater.* **30**, 1802661 (2018)
47. L. Edman, Ion association and ion solvation effects at the crystalline-amorphous phase transition in PEO-LiTFSI. *J. Phys. Chem. B* **104**, 7254–7258 (2000)
48. I. Rey, P. Johansson, J. Lindgren, J.C. Lassègues, J. Grondin, L. Servant, Spectroscopic and theoretical study of (CF₃SO₂)₂N⁻ (TFSI⁻) and (CF₃SO₂)₂NH (HTFSI). *J. Phys. Chem. A* **102**, 3249–3258 (1998)
49. C. Ma, K. Dai, H. Hou, X. Ji, L. Chen, D.G. Ivey, W. Wei, High ion-conducting solid-state composite electrolytes with carbon quantum dot nanofillers. *Adv. Sci.* **5**, 1700996 (2018)
50. J. Ma, B. Chen, L. Wang, G. Cui, Progress and prospect on failure mechanisms of solid-state lithium batteries. *J. Power Sour.* **392**, 94–115 (2018)
51. B.J. Xiao, How lithium dendrites form in liquid batteries. *Sci.* **366**, 426–428 (2019)
52. Q. Zhang, K. Liu, F. Ding, X. Liu, Recent advances in solid polymer electrolytes for lithium batteries. *Nano Res.* **10**, 4139–4174 (2017)
53. W. Wu, Y. Li, J. Liu, J. Wang, Y. He, K. Davey, S.Z. Qiao, Molecular-level hybridization of Nafion with quantum dots for highly enhanced proton conduction. *Adv. Mater.* **30**, 1707516 (2018)
54. Q. Lu, Y.B. He, Q. Yu, B. Li, Y.V. Kaneti, Y. Yao, F. Kang, Q.H. Yang, Dendrite-free, high-rate, long-life lithium metal batteries with a 3D cross-linked network polymer electrolyte. *Adv. Mater.* **29**, 1604460 (2017)
55. Y. Zhu, J. Cao, H. Chen, Q. Yu, B. Li, High electrochemical stability of a 3D cross-linked network PEO@nano-SiO₂ composite polymer electrolyte for lithium metal batteries. *J. Mater. Chem. A* **7**, 6832–6839 (2019)
56. Z. Xiao, B. Zhou, J. Wang, C. Zuo, D. He, X. Xie, Z. Xue, PEO-based electrolytes blended with star polymers with precisely imprinted polymeric pseudo-crown ether cavities for alkali metal ion batteries. *J. Membr. Sci.* **576**, 182–189 (2019)
57. J. Hu, W. Wang, B. Zhou, Y. Feng, X. Xie, Z. Xue, Poly (ethylene oxide)-based composite polymer electrolytes embedding with ionic bond modified nanoparticles for all-solid-state lithium-ion battery. *J. Membr. Sci.* **575**, 200–208 (2019)

58. X. Zhou, H. Jiang, H. Zheng, Y. Sun, X. Liang, H. Xiang, Nonflammable hybrid solid electrolyte membrane for a solid-state lithium battery compatible with conventional porous electrodes. *J. Membr. Sci.* **603**, 117820 (2020)
59. L. Liu, J. Lyu, J. Mo, H. Yan, L. Xu, P. Peng, J. Li, B. Jiang, L. Chu, M. Li, Comprehensively-upgraded polymer electrolytes by multifunctional aramid nanofibers for stable all-solid-state Li-ion batteries. *Nano Energy* **69**, 104398 (2020)
60. Z. Zou, Y. Li, Z. Lu, D. Wang, Y. Cui, B. Guo, Y. Li, X. Liang, J. Feng, H. Li, C.W. Nan, M. Armand, L. Chen, K. Xu, S. Shi, Mobile ions in composite solids. *Chem. Rev.* **120**, 4169–4221 (2020)
61. N.S. Murthy, H. Minor, General procedure for evaluating amorphous scattering and crystallinity from X-ray diffraction scans of semicrystalline polymers. *Polymer* **31**, 996–1002 (1989)
62. T.H. Lee, F.Y.C. Boey, K.A. Khor, X-ray diffraction analysis technique for determining the polymer crystallinity in a polyphenylene sulfide composite. *Polym. Compos.* **16**, 481–488 (1995)
63. N. Lago, O. Garcia-Calvo, J.M. Lopezdelamo, T. Rojo, M. Armand, All-solid-state lithium-ion batteries with grafted ceramic nanoparticles dispersed in solid polymer electrolytes. *Chemsuschem* **8**, 3039–3043 (2015)
64. S. Li, K. Jiang, J. Wang, C. Zuo, Y.H. Jo, D. He, X. Xie, Z. Xue, Molecular brush with dense PEG side chains: design of a well-defined polymer electrolyte for lithium-ion batteries. *Macromolecules* **52**, 7234–7243 (2019)
65. Q. Zhou, J. Ma, S. Dong, X. Li, G. Cui, Intermolecular chemistry in solid polymer electrolytes for high-energy-density lithium batteries. *Adv. Mater.* **31**, 1902029 (2019)
66. Z. Wang, X. Huang, L. Chen, Understanding of effects of nano- Al_2O_3 particles on ionic conductivity of composite polymer electrolytes. *Electrochem. Solid-State Lett.* **6**, E40–E44 (2003)
67. T. Li, P. Shi, R. Zhang, H. Liu, X.B. Cheng, Q. Zhang, Dendrite-free sandwiched ultrathin lithium metal anode with even lithium plating and stripping behavior. *Nano Res.* **12**, 2224–2229 (2019)
68. J. Wang, M. Li, C. Liu, Y. Liu, T. Zhao, P. Zhai, J. Wang, An electronegative modified separator with semifused pores as a selective barrier for highly stable lithium-sulfur batteries. *Ind. Eng. Chem. Res.* **58**, 14538–14547 (2019)
69. J. Zhang, C. Ma, Q. Xia, J. Liu, Z. Ding, M. Xu, L. Chen, W. Wei, Composite electrolyte membranes incorporating viscous copolymers with cellulose for high performance lithium-ion batteries. *J. Membr. Sci.* **497**, 259–269 (2016)
70. Z. Xie, Z. Wu, X. An, X. Yue, P. Xiaokaiti, A. Yoshida, A. Abudula, G. Guan, A sandwich-type composite polymer electrolyte for all-solid-state lithium metal batteries with high areal capacity and cycling stability. *J. Membr. Sci.* **596**, 117739 (2020)
71. S. Zhao, Y. Wang, J. Dong, C.T. He, H. Yin, P. An, K. Zhao, X. Zhang, C. Gao, L. Zhang, J. Lv, J. Wang, J. Zhang, A.M. Khattak, N.A. Khan, Z. Wei, J. Zhang, S. Liu, H. Zhao, Z. Tang, Ultrathin metal-organic framework nanosheets for electrocatalytic oxygen evolution. *Nat. Energy* **1**, 16184 (2016)
72. Y. Wang, Y. Liu, H. Wang, W. Liu, Y. Li, J. Zhang, H. Hou, J. Yang, Ultrathin NiCo-MOF Nanosheets for High-Performance Supercapacitor Electrodes. *ACS Appl. Energy Mater.* **2**, 2063–2071 (2019)
73. Z. Guo, Y. Zhang, Y. Dong, J. Li, S. Li, P. Shao, X. Feng, B. Wang, Fast ion transport pathway provided by polyethylene glycol confined in covalent organic frameworks. *J. Am. Chem. Soc.* **141**, 1923–1927 (2019)
74. H. Deng, C.J. Doonan, H. Furukawa, R.B. Ferreira, J. Towne, C.B. Knobler, B. Wang, O.M. Yaghi, Multiple functional groups of varying ratios in metal-organic frameworks. *Science* **327**, 846–850 (2010)
75. M. Eddaoudi, J. Kim, N. Rosi, D. Vodak, J. Wachter, M. O’Keeffe, O.M. Yaghi, Systematic design of pore size and functionality in isorecticular MOFs and their application in methane storage. *Science* **295**, 469–472 (2002)

76. S. Yuan, L. Huang, Z. Huang, D. Sun, J.S. Qin, L. Feng, J. Li, X. Zou, T. Cagin, H.C. Zhou, Continuous variation of lattice dimensions and pore sizes in metal–organic frameworks. *J. Am. Chem. Soc.* **142**, 4732–4738 (2020)
77. H. Qin, K. Fu, Y. Zhang, Y. Ye, M. Song, Y. Kuang, S.H. Jang, F. Jiang, L. Cui, Flexible nanocellulose enhanced Li^+ conducting membrane for solid polymer electrolyte. *Energy Storage Mater.* **28**, 293–299 (2020)
78. X. Zhang, J. Xie, F. Shi, D. Lin, Y. Liu, W. Liu, A. Pei, Y. Gong, H. Wang, K. Liu, Y. Xiang, Y. Cui, Vertically aligned and continuous nanoscale ceramic–polymer interfaces in composite solid polymer electrolytes for enhanced ionic conductivity. *Nano Lett.* **18**, 3829–3838 (2018)
79. S. Ramesh, T.F. Yuen, C.J. Shen, Conductivity and FTIR studies on PEO–LiX [X: CF_3SO_3^- , SO_4^{2-}] polymer electrolytes. *Spectrochim. Acta Part A Mol. Biomol. Spectrosc.* **69**, 670–675 (2008)
80. L.H. Sim, S.N. Gan, C.H. Chan, R. Yahya, ATR-FTIR studies on ion interaction of lithium perchlorate in polyacrylate/poly (ethylene oxide) blends. *Spectrochim. Acta Part A Mol. Biomol. Spectrosc.* **76**, 287–292 (2010)
81. M. Marcinek, M. Ciosek, G. Zukowska, W. Wieczorek, K.R. Jeffrey, J.R. Stevens, The impact of end groups on ionic interactions in low molecular weight Al_2O_3 –polyether– LiClO_4 electrolytes. *Solid State Ionics* **171**, 69–80 (2004)
82. Y. Suzuki, H. Duran, M. Steinhart, H.J. Butt, G. Floudas, Homogeneous crystallization and local dynamics of poly (ethylene oxide) (PEO) confined to nanoporous alumina. *Soft Matter* **9**, 2621–2628 (2013)
83. H. Huo, B. Wu, T. Zhang, X. Zheng, L. Ge, T. Xu, X. Guo, X. Sun, Anion-immobilized polymer electrolyte achieved by cationic metal-organic framework filler for dendrite-free solid-state batteries. *Energy Storage Mater.* **18**, 59–67 (2019)
84. Z. Yang, H. Yuan, C. Zhou, Y. Wu, W. Tang, S. Sang, H. Liu, Facile interfacial adhesion enabled LAMP-based solid-state lithium metal battery. *Chem. Eng. J.* **392**, 123650 (2020)
85. R. Li, S. Guo, L. Yu, L. Wang, D. Wu, Y. Li, X. Hu, Morphosynthesis of 3D macroporous garnet frameworks and perfusion of polymer-stabilized lithium salts for flexible solid-state hybrid electrolytes. *Adv. Mater. Interfaces* **6**, 1900200 (2019)
86. Z. Wan, D. Lei, W. Yang, C. Liu, K. Shi, X. Hao, L. Shen, W. Lv, B. Li, Q.H. Yang, F. Kang, Y.B. He, Low resistance-integrated all-solid-state battery achieved by $\text{Li}_7\text{La}_3\text{Zr}_2\text{O}_{12}$ nanowire upgrading polyethylene oxide (PEO) composite electrolyte and PEO cathode binder. *Adv. Func. Mater.* **29**, 1805301 (2019)
87. J. Bae, Y. Li, J. Zhang, X. Zhou, F. Zhao, Y. Shi, J.B. Goodenough, G. Yu, A 3D nanostructured hydrogel-framework-derived high-performance composite polymer lithium-ion electrolyte. *Angew. Chem. Int. Ed.* **57**, 2096–2100 (2018)
88. C.Z. Zhao, X.Q. Zhang, X.B. Cheng, R. Zhang, R. Xu, P.Y. Chen, H.J. Peng, J.Q. Huang, Q. Zhang, An anion-immobilized composite electrolyte for dendrite-free lithium metal anodes. *Proc. Natl. Acad. Sci.* **114**, 11069–11074 (2017)
89. J. Zheng, M. Tang, Y.Y. Hu, Lithium ion pathway within $\text{Li}_7\text{La}_3\text{Zr}_2\text{O}_{12}$ polyethylene oxide composite electrolytes. *Angew. Chem. Int. Ed.* **128**, 12726–12730 (2016)
90. N. Wu, P.H. Chien, Y. Qian, Y. Li, H. Xu, N.S. Grundish, B. Xu, H. Jin, Y.Y. Hu, G. Yu, J.B. Goodenough, Enhanced surface interactions enable fast Li^+ conduction in oxide/polymer composite electrolyte. *Angew. Chem. Int. Ed.* **59**, 4131–4137 (2020)
91. K. He, J. Zha, P. Du, S. H. Cheng, C. Liu, Z. Dang, R.K.Y. Li, Tailored high cycling performance in a solid polymer electrolyte with perovskite-type $\text{Li}_{0.33}\text{La}_{0.557}\text{TiO}_3$ nanofibers for all-solid-state lithium ion batteries. *Dalton Trans.* **48**, 3263–3269 (2019)
92. P. Zhu, C. Yan, M. Dirican, J. Zhu, J. Zang, R.K. Selvan, C.C. Chung, H. Jia, Y. Li, Y. Kiyak, N. Wu, X. Zhang, $\text{Li}_{0.33}\text{La}_{0.557}\text{TiO}_3$ ceramic nanofiber-enhanced polyethylene oxide-based composite polymer electrolytes for all-solid-state lithium batteries. *J. Mater. Chem. A*, **6**, 4279–4285 (2018)
93. Y. Zhao, S. Hao, L. Su, Z. Ma, G. Shao, Hierarchical Cu fibers induced Li uniform nucleation for dendrite-free lithium metal anode. *Chem. Eng. J.* **392**, 123691 (2020)

94. J. Wan, J. Xie, X. Kong, Z. Liu, K. Liu, F. Shi, A. Pei, H. Chen, W. Chen, J. Chen, X. Zhang, L. Zong, J. Wang, L. Chen, J. Qin, Y. Cui, Ultrathin, flexible, solid polymer composite electrolyte enabled with aligned nanoporous host for lithium batteries. *Nat. Nanotechnol.* **14**, 705–711 (2019)
95. T. Jiang, P. He, G. Wang, Y. Shen, C.W. Nan, L.Z. Fan, Solvent-free synthesis of thin, flexible, nonflammable garnet-based composite solid electrolyte for all-solid-state lithium batteries. *Adv. Energy Mater.* **10**, 1903376 (2020)
96. A.A. AbdelHamid, J.L. Cheong, J.Y. Ying, $\text{Li}_7\text{La}_3\text{Zr}_2\text{O}_{12}$ sheet-based framework for high-performance lithium-sulfur hybrid quasi-solid battery. *Nano Energy* **71**, 104633 (2020)
97. W. Li, C. Sun, J. Jin, Y. Li, C. Chen, Z. Wen, Realization of the Li^+ domain diffusion effect via constructing molecular brushes on the LLZTO surface and its application in all-solid-state lithium batteries. *J. Mater. Chem. A* **7**, 27304–27312 (2019)
98. K.J. Kim, M. Balaish, M. Wadaguchi, L. Kong, J.L.M. Rupp, Solid-state Li-metal batteries: challenges and horizons of oxide and sulfide solid electrolytes and their interfaces. *Adv. Energy Mater.* **11**, 2002689 (2021)
99. Z. Jiang, S. Wang, X. Chen, W. Yang, X. Yao, X. Hu, Q. Han, H. Wang, Tape-casting $\text{Li}_{0.34}\text{La}_{0.56}\text{TiO}_3$ ceramic electrolyte films permit high energy density of lithium-metal batteries. *Adv. Mater.* **32**, 1906221 (2020)
100. S. Jung, H. Gwon, G. Yoon, L.J. Miara, V. Lacivita, J. Kim, Pliable lithium superionic conductor for all-solid-state batteries. *ACS Energy Lett.* **6**, 2006–2015 (2021)
101. X. Yang, K.R. Adair, X. Gao, X. Sun, Recent advances and perspectives on thin electrolytes for high-energy-density solid-state lithium batteries. *Energy Environ. Sci.* **14**, 643–671 (2021)
102. J. Wu, L. Yuan, W. Zhang, Z. Li, X. Xie, Y. Huang, Reducing the thickness of solid-state electrolyte membranes for high-energy lithium batteries. *Energy Environ. Sci.* **14**, 12–36 (2021)
103. N. Zhao, W. Khokhar, Z. Bi, C. Shi, X. Guo, L.Z. Fan, C.W. Nan, Solid garnet batteries. *Joule* **3**, 1190–1199 (2019)
104. X. Chen, W. He, L.X. Ding, S. Wang, H. Wang, Enhancing interfacial contact in all solid state batteries with a cathode-supported solid electrolyte membrane framework. *Energy Environ. Sci.* **12**, 938–944 (2019)
105. H. Huo, X. Li, Y. Sun, X. Lin, K.D. Davis, J. Liang, X. Gao, R. Li, H. Huang, X. Guo, X. Sun, Li_2CO_3 effects: new insights into polymer/garnet electrolytes for dendrite-free solid lithium batteries. *Nano Energy* **73**, 104836 (2020)
106. J.J. Shao, K. Raidongia, A.R. Koltonow, J. Huang, Self-assembled two-dimensional nanofluidic proton channels with high thermal stability. *Nat. Commun.* **6**, 7602 (2015)
107. C.H. Chen, J. Du, Lithium ion diffusion mechanism in lithium lanthanum titanate solid-state electrolytes from atomistic simulations. *J. Am. Ceram. Soc.* **98**, 534–542 (2014)
108. X. Wang, H. Wang, Y. Zhou, Y. Liu, B. Li, X. Zhou, H. Shen, Confined-space synthesis of single crystal TiO_2 nanowires in atmospheric vessel at low temperature: a generalized approach. *Sci. Rep.* **5**, 8129 (2015)
109. X. Gao, C.A.J. Fisher, T. Kimura, Y.H. Ikuhara, H. Moriwake, A. Kuwabara, H. Oki, T. Tojigamori, R. Huang, Y. Ikuhara, Lithium atom and A-site vacancy distributions in lanthanum lithium titanate. *Chem. Mater.* **25**, 1607–1614 (2013)
110. A.A. AbdelHamid, Y. Yu, J. Yang, J.Y. Ying, Generalized synthesis of metal oxide nanosheets and their application as Li-ion battery anodes. *Adv. Mater.* **29**, 1701427 (2017)
111. M. Romero, R. Faccio, S. Vázquez, S. Davyt, Á. W. Mombrú, Experimental and theoretical Raman study on the structure and microstructure of $\text{Li}_{0.30}\text{La}_{0.57}\text{TiO}_3$ electrolyte prepared by the sol-gel method in acetic medium. *Ceram. Int.* **42**, 15414–15422 (2016)
112. M.J. Wang, J.B. Wolfenstine, J. Sakamoto, Mixed electronic and ionic conduction properties of lithium lanthanum titanate. *Adv. Func. Mater.* **30**, 1909140 (2020)